The abundances of F, Cl, and H_2O in eucrites: Implications for the origin of volatile depletion in the asteroid 4 Vesta

Francis M. McCubbin[1], Jonathan A. Lewis[1], Jessica J. Barnes[2], Stephen M. Elardo[3], and Jeremy W. Boyce[1]

[1]NASA Johnson Space Center, Mailcode XI2, 2101 NASA Parkway, Houston, Texas 77058, USA

[2]Lunar and Planetary Laboratory, University of Arizona, 1629 E University Blvd, Tucson, AZ 85721, USA

[3]Department of Geological Sciences, University of Florida, Gainesville, FL 32611, USA

Abstract

We conducted a petrologic study of apatite within eight unbrecciated, non-cumulate eucrites and two monomict, non-cumulate eucrites. These data were combined with previously published data to quantify the abundances of F, Cl, and H_2O in the bulk silicate portion of asteroid 4 Vesta (BSV). Using a combination of apatite-based melt hygrometry/chlorometry and appropriately paired volatile/refractory element ratios, we determined that BSV has 3.0–7.2 ppm F, 0.39–1.8 ppm Cl, and 3.6–22 ppm H_2O. The abundances of F and H_2O are depleted in BSV relative to CI chondrites to a similar degree as F and H_2O in the bulk silicate portion of the Moon. This degree of volatile depletion in BSV is similar to what has been determined previously for many moderately volatile elements in 4 Vesta (e.g., Na, K, Zn, Rb, Cs, and Pb). In contrast, Cl is depleted in 4 Vesta by a greater degree than what is recorded in samples from Earth or the Moon. Based on the Cl-isotopic compositions of eucrites and the bulk rock Cl/F ratios determined in this study, the eucrites likely formed through serial magmatism of a mantle with heterogeneous $\delta^{37}Cl$ and Cl/F, not as extracts from a partially crystallized global magma ocean. Furthermore, the volatile depletion and Cl-isotopic heterogeneity recorded in eucrites is likely inherited, at least in part, from the precursor materials that accreted to form 4 Vesta and is unlikely to have resulted solely from degassing of a global magma ocean, magmatic degassing of eucrite melts, and/or volatile loss during thermal metamorphism. Although our results can be reconciled with the past presence of wide-scale melting on 4 Vesta (i.e., a partial magma ocean), any future models for eucrite petrogenesis involving a global magma ocean would need to account for the preservation of a heterogeneous eucrite source with respect to Cl/F ratios and Cl isotopes.

1.0 INTRODUCTION

The abundances and distributions of magmatic volatiles within the silicate portions of differentiated planetary bodies, including terrestrial planets, moons, and asteroids, have profound consequences on their subsequent thermochemical evolution. Magmatic volatile elements, including H, C, N, F, S, and Cl, are a subset of volatile elements that are of critical importance to a wide range of geological and biological processes (e.g., Campbell and Taylor, 1983; Persikov et al., 1990; Hirth and Kohlstedt, 1996; Gaetani and Grove, 1998; Aiuppa et al., 2009; Ehlmann et al., 2016; Westall and Brack, 2018). The abundances of magmatic volatiles within the silicate portions of differentiated planetary bodies are difficult to quantify because they are depleted by varying degrees relative to CI chondrites (e.g., Albarède, 2009). The mechanisms of depletion are not well constrained and could relate to intrinsic volatile depletion of the building blocks that condensed from the nebula and protoplanetary disk, high temperature processes that result from accretion, post-accretion loss through parent body geological processes and large-scale impacts, and/or redistribution within a parent body through processes like core formation (Boss, 1998; Chambers, 2004; Moynier et al., 2011; Sharp et al., 2013a; Chi et al., 2014; Albarède et al., 2015; Canup et al., 2015; Norris and Wood, 2017; Sutton et al., 2017; Nakajima and Stevenson, 2018; Lin and van Westrenen, 2019; McCubbin and Barnes, 2019; Righter, 2019; Steenstra et al., 2019, 2020). Furthermore, there is substantial debate as to the timing of volatile arrival to the terrestrial bodies of the inner Solar System, particularly with respect to H_2O, with models ranging from its presence at the initial stages of accretion to late delivery by comets and/or asteroids (Raymond et al., 2004; Drake, 2005; Albarède, 2009, 2013; Greenwood et al., 2011; Marty, 2012; McCubbin et al., 2012; Sarafian et al., 2014, 2017a; Barnes et al., 2016a; Sharp, 2017; Alexander et al., 2018;

O'Brien et al., 2018; Wu et al., 2018; McCubbin and Barnes, 2019). To place better constraints on the presence of volatiles in the inner Solar System within its first 4 million years (defined by the formation of calcium-aluminum-rich inclusions (CAI) at 4567.30 ± 0.16 Ma; Connelly et al., 2012), we aim to determine the abundances of volatiles in the ancient differentiated asteroid 4 Vesta.

The asteroid 4 Vesta is a differentiated planetary embryo within the inner asteroid belt that is one of only a handful of embryos that survived the process of planet formation (Russell et al., 2012). It is not clear whether 4 Vesta accreted within the protoplanetary disk near its present orbit (~2.36 AU) or accreted closer to the Sun and moved outward at a later time (Bottke et al., 2006; Zuber et al., 2011). Dynamical models suggest that material excavated from 4 Vesta can be delivered to Earth as meteorites (Binzel and Xu, 1993), and there are strong spectral similarities linking 4 Vesta to the howardite, eucrite, and diogenite (HED) meteorites (McCord et al., 1970; Burbine et al., 2001; McSween et al., 2011). Evaluation of the asteroid 4 Vesta by NASA's Dawn spacecraft provided further evidence linking HED meteorites to 4 Vesta (Russell et al., 2012; McSween et al., 2013; Mittlefehldt, 2015). The Dawn Mission confirmed the presence of a metallic Fe-rich core in 4 Vesta, and ^{182}Hf–^{182}W, ^{60}Fe–^{60}Ni, ^{53}Mn–^{53}Cr, ^{26}Al–^{26}Mg, and initial ^{87}Sr/^{86}Sr systematics of HED meteorites indicate that core formation on their parent body occurred within the first 4 million years of CAI formation and possibly within the first million years (Lugmair and Shukolyukov, 1998; Trinquier et al., 2008; Kleine et al., 2009; Tang and Dauphas, 2012; Touboul et al., 2015; Hublet et al., 2017). The differentiation of 4 Vesta occurred while ^{26}Al was extant, and the homogeneity in Δ^{17}O compositions of HED meteorites support the idea that 4 Vesta may have differentiated via a magma ocean (Greenwood et al., 2005). In the magma ocean model, eucrites and diogenites are thought to be products of the magma ocean (Righter and Drake, 1997;

Ruzicka et al., 1997; Warren, 1997; Greenwood et al., 2005; Mandler and Elkins-Tanton, 2013); however, some models point to serial magmatism as the origin of eucrites and diogenites (Stolper, 1977; Fowler et al., 1995; Yamaguchi et al., 1996; Shearer et al., 2010; Kumler and Day, 2021). Crystallization ages of basaltic eucrites indicate that crust formation on 4 Vesta was completed within 8 Myr of CAI formation (Srinivasan et al., 2007), although magmatism and/or thermal metamorphism occurred on 4 Vesta for up to 50 Myr after CAI (Misawa et al., 2005; Zhou et al., 2013; Bouvier et al., 2015; Hopkins et al., 2015). Given the rapid accretion and differentiation of 4 Vesta, it could provide valuable insights into the availability and retention of volatiles in protoplanets at the earliest stages of inner Solar System history.

Both the HED meteorites and data from Dawn indicate that 4 Vesta is depleted in moderately volatile elements relative to the terrestrial planets (Dreibus and Wänke, 1980; Beck et al., 2015; Mittlefehldt, 2015; Prettyman et al., 2015). In fact, the magnitude of volatile depletion on 4 Vesta is purported to be similar to (but not as severe as) the Moon (Dreibus and Wänke, 1980; Gillis et al., 2004; Prettyman et al., 2006; Lawrence et al., 2007; Hauri et al., 2015). Estimates for the interior oxygen fugacity (fO_2) of 4 Vesta relative to the iron-wüstite (IW) buffer range from ΔIW-1 to ΔIW-4 based on eucrite geochemistry and estimated core compositions (Stolper, 1977; Righter and Drake, 1996; Pringle et al., 2013; Steenstra et al., 2016); however, on the basis of metal-silicate partitioning for a wide range of elements, estimates near ΔIW-2 are considered most reasonable for the conditions of core formation (Righter and Drake, 1996; Steenstra et al., 2016). The volatile depletion of 4 Vesta and its low oxygen fugacity both supported earlier ideas that 4 Vesta is dry (e.g., Palme, 2000; Patiño Douce and Roden, 2006). However, the discovery of H_2O in lunar samples (Saal et al., 2008; Boyce et al., 2010; McCubbin et al., 2010a; Hauri et al., 2011) invigorated the search for H_2O in other reduced and volatile depleted bodies such as 4 Vesta, and

the presence of H_2O in the interior of 4 Vesta was confirmed by the analysis of apatite [$Ca_5(PO_4)_3(F,Cl,OH)$] and nominally anhydrous minerals within eucrites (Sarafian et al., 2013, 2014, 2017b, 2019; Barrett et al., 2016, 2021; Stephant et al., 2021).

In the present study, we aim to constrain the abundances of F, Cl, and H_2O in eucrite sources, which are then compared with the abundances of other volatile and moderately volatile elements to assess the degree to which 4 Vesta is depleted in volatiles and to glean what processes might be responsible for volatile depletion. To accomplish these objectives, we report electron microprobe analyses of apatite from seven unbrecciated, non-cumulate eucrites and two monomict, non-cumulate eucrites. In combination with previously published data on eucrite-hosted apatite, we determine Cl/F and H_2O/F ratios in bulk rock eucrites through the application of apatite-based melt hygrometry and chlorometry (e.g., Boyce et al., 2014; McCubbin et al., 2015b; McCubbin and Ustunisik, 2018). Furthermore, we estimate the bulk rock abundances of F in six non-cumulate eucrites, which we combine with previously published bulk rock F data on non-cumulate eucrites (Dreibus et al., 1979; Kitts and Lodders, 1998; Lodders and Fegley, 1998; Mittlefehldt, 2015) to constrain the abundances of F, Cl, and H_2O in 4 Vesta using appropriately paired volatile/refractory element ratios for F, followed by Cl/F and H_2O/F ratios for Cl and H_2O, respectively (e.g., Saal et al., 2002; Salters and Stracke, 2004; Ni et al., 2019).

2.0 METHODS

Petrographic and/or chemical (electron probe microanalysis) data were collected on thin sections from 10 different eucrites from the Institute of Meteoritics (IOM) at the University of New Mexico (UNM) (Berthoud), the Naturhistorisches Museum in Vienna (Stannern), and the United States Antarctic Meteorite Collection at NASA Johnson Space Center (JSC)/Smithsonian Institution (Cumulus Hills (CMS) 04049, Graves Nunataks (GRA) 98098, Lewis Cliff (LEW)

88010, MacAlpine Hills (MAC) 02522, MAC 041169, Pecora Escarpment (PCA) 91078, Queen Alexandra Range (QUE) 94484, and QUE 97053). These data were combined with literature data on a broader set of eucrites, and a complete list of all the meteorites considered in this study, as well as their petrologic type and geochemical classification, is provided in Table 1.

2.1. Imaging analysis

Back-scattered electron (BSE) images were acquired using the JEOL JXA 8200 electron microprobe in the Institute of Meteoritics (IOM) at the University of New Mexico (UNM) and using the JEOL 8530 field emission electron microprobe housed within the Astromaterials Research and Exploration Science (ARES) Division at NASA Johnson Space Center (JSC). The BSE images were collected using a 15 kV accelerating voltage and 20 nA beam current.

Full-section BSE and energy-dispersive X-ray spectroscopy (EDS) maps were collected using a JEOL 7600F field emission scanning electron microscope (FE-SEM) housed within ARES at NASA JSC. The FE-SEM was operated using a 15 kV accelerating voltage. Most maps were collected using a 30 nA beam, magnification between 110x and 120x, 5–10% tile overlap, dwell time of 10–12 ms/px, and tile size of 256×192 px with resolutions of 3.8–4.1 μm/px. The Berthoud (Figure 1b) map was collected using a 10 nA beam and a dwell time of 30 ms/px resulting in an equivalent signal to the 30 nA maps. Individual BSE tiles were stitched together using the ImageJ software with the Grid/Collection stitching plugin (Preibisch et al., 2009). The plugin computed the overlap of the individual tiles which compensated for inaccuracies in SEM stage positioning. The EDS data cubes for each tile were converted to element images by summing the counts per pixel in each of the EDS channels representing a 10% window around the Kα X-ray energy peak for each element (i.e., the eV for that element ±5%). This relatively broad window allows for an increase in signal, but it sacrifices the ability to differentiate between overlapping elements (e.g.,

P Kα and Zr Lα). The tiles for each element map were stitched using the stitch position file generated from the BSE map, creating a perfect alignment between each element map and the BSE map. Phase maps were generated using P, Si, Ti, Al, Cr, Ca, Mg, S, and C element maps by creating element-element plots and determining the characteristic X-ray counts for each element within each phase of interest. Each pixel of the map was assigned a phase based on the X-ray counts for each element. Phosphates were determined by high P and Ca counts to distinguish them from Zircon which have high Zr (peak overlapping with P), but low Ca counts. Merrillite was distinguished against apatite through higher Mg counts. Glass (fusion crust and melt) was distinguished by having low P and S and intermediate amounts of Si, Al, and Ca that differed from the major mineralogy. Epoxy was determined using high C counts and low BSE intensity. For most maps, fewer than 1% of the pixels were unassigned; however, the maps for Berthoud (Figures 1a and 1c) have more unassigned pixels (1–2%) due to topography within the samples. The phase maps were then checked against the BSE maps and, for the phosphates, against subsequent SEM imaging to ensure accuracy of grain identification. Modal mineralogy was calculated as the sum of the pixels for each phase as a percentage of all assigned pixels omitting glass, epoxy, and unassigned pixels. The calculated modal mineralogy is considered as the volume abundance of each mineral in each section.

2.1.1. Estimation of bulk rock F abundances in eucrites

We computed bulk rock abundances of F within GRA 98098, MAC 041169, PCA 91078, QUE 97053, Stannern, and Berthoud based on our determination of modal mineralogy in those samples. Fluorine abundance estimates assume that apatite is the only mineral that meaningfully contributes to the bulk rock inventory of F, which is supported by the low abundances of F in nominally fluorine-free minerals in eucrites (i.e., ≤0.23 ppm F in pyroxene; Sarafian et al., 2019)

and the inability of F to be incorporated into whitlockite-merrillite group minerals (McCubbin et al., 2018). Although a novel approach to estimate F in eucrites, modal abundances of apatite have been used to estimate bulk rock abundances of F in some ordinary chondrites (Lewis and Jones, 2016).

To compute bulk rock fluorine abundances, we use the modal mineralogy and average apatite compositions for each sample. Our mineral modes are based on percent volume, so we converted the volume modes to mass-based modes using the densities of each of the minerals. The mineral densities were all computed based on unit cell parameters using reported mineral compositions from each eucrite sample for low-Ca pyroxene, high-Ca pyroxene, plagioclase, and apatite (i.e., Basaltic Volcanism Study Project, Meteoritical Bulletin Database, Table 2). Densities for baddeleyite, zircon, Ca-merrillite, tridymite, troilite, chromite, and ilmenite were computed on the basis of endmember compositions.

2.2. Electron probe microanalysis (EPMA)

Electron Probe microanalysis (EPMA) of apatite in the eucrites CMS 04049, GRA 98098, LEW 88010, MAC 02522, MAC 041169, QUE 94484, and QUE 97053 was conducted using a JEOL JXA 8200 electron microprobe equipped with 5 wavelength dispersive spectrometers in the IOM at UNM. Data were collected using both the JEOL manufacturer's software and the Probe for EPMA (PFE) software from Probe Software, Inc. Electron Probe microanalysis (EPMA) of apatite in the eucrites Berthoud and Stannern was conducted using a JEOL 8530 field emission electron microprobe housed in ARES at NASA JSC. Data were collected using PFE software from Probe Software, Inc. All apatite was analyzed using a 15 kV accelerating voltage and 20 nA beam current following previous procedures established by our group for the analysis of apatite in planetary materials (e.g., McCubbin et al., 2010b, 2011). For all samples, F was analyzed using a

light-element LDE1 diffraction crystal, and Cl was analyzed using a PET diffraction crystal. In order to reduce or eliminate electron beam damage, we used a 10 µm spot for standardization and 1 to 10 µm diameter beams for analysis of apatite grains in all the eucrites. Furthermore, we conducted wavelength scans on subsets of apatite within eucrites to identify appropriate F peak positions and background positions, notably to avoid interferences from Fe$L\alpha_1$ and Fe$L\beta_1$ X-ray lines (Potts and Tindle, 1989; Witter and Kuehner, 2004) in the Fe-bearing eucrite apatite. Although the shoulder on the Fe$L\alpha_1$ peak can overlap slightly with the F$K\alpha$ peak, the largest contribution of false F counts that is possible from Fe in the eucrite apatite (i.e., apatite in eucrites have ≤3.2 wt.% FeO; Tables S1–S9) equates to ≤0.012 wt% F (Potts and Tindle, 1989), which is within our analytical uncertainty.

For apatite in the eucrites CMS 04049, GRA 98098, LEW 88010, MAC 02522, MAC 041169, QUE 94484, and QUE 97053, we analyzed the elements P, Si, Ce, Y, Fe, Mn, Mg, Ca, Na, F, Cl, and S. The standards used for calibration include: Durango apatite (Jarosewich et al., 1980) and Wilberforce apatite (from the Taylor multi element standard mount from C.M. Taylor) for Ca and P, and a natural fluorapatite from India (Ap020 from McCubbin et al., 2012) was used as a secondary check on the standardization. A synthetic SrF_2 crystal from the Taylor multi element standard mount was used as the primary F standard, and Ap020 was used as an additional check on the F standardization. A synthetic sodalite crystal (from Sharp et al., 1989) was used as a primary Cl standard, and scapolite from the Smithsonian (UNNM R6600-1) was used as a secondary check on the Cl standardization. Barite from the Taylor multi element standard mount was used as the primary S standard, and scapolite from the Smithsonian (UNNM R6600-1) was used as a secondary S standard. Albite, wollastonite, and diopside from the Taylor multi element standard mount were used as a primary standard for Na, Si, and Mg, respectively. Ilmenite from

the Smithsonian (USNM 133868) was used as a primary standard for Fe and Mn. Cerium and Y were standardized using their respective synthetic orthophosphate endmembers from Jarosewich and Boatner (1991).

For apatite in the eucrites Stannern and Berthoud, we analyzed the elements P, Si, Fe, Mn, Mg, Ca, Na, F, Cl, and S. The standards used for calibration include: Durango apatite (Jarosewich et al., 1980) and fluourapatite (from SPI Supplies) for Ca and P, and Ap020 was used as secondary check on the standardization. A synthetic SrF_2 crystal was used as the primary F standard, and Ap020 was used as an additional check on the F standardization. Tugtupite (from SPI Supplies) was used as a primary Cl standard. Barite (from SPI Supplies) was used as the primary S standard. Albite (from SPI Supplies) was used as a primary standard for Na, and diopside (from SPI Supplies) was used as a primary standard for Si. Ilmenite from the Smithsonian (USNM 96189) was used as a primary standard for Fe, and Mn was standardized using rhodonite (from SPI Supplies).

Hydroxyl cannot be measured by the electron microprobe; however, a missing component in the X-site of apatite can be calculated on the basis of stoichiometry if both F and Cl are analyzed with sufficient accuracy. The missing component can be attributed to some combination of the anions OH^-, O^{2-}, CO_3^{2-}, S^{2-}, Br^-, and I^- and/or structural vacancies (Pan and Fleet, 2002) and/or structural H_2O (Mason et al., 2009). Estimating a missing component with accuracy is often challenging because fluorine and chlorine X-ray count rates can vary over the course of an electron microprobe analysis of apatite (Stormer et al., 1993). We monitored the apatite analyses for time-dependent count rates and discovered that fluorine count rates were variable during the course of some analyses. We did not observe any variation in the Cl X-ray count rates for any of our apatite analyses, consistent with our previous work on apatite (e.g., McCubbin et al., 2016). For the

analyses that exhibited variable F X-ray count variation, we used a time-dependent intensity (TDI) correction in the PFE software using the methods described in McCubbin et al. (2010b). Any analyses that displayed highly variable fluorine X-ray count rates or non-linear and non-positive changes in F X-ray count rates during the course of an analysis were rejected. Even with this criterion, some of the apatite contained more F + Cl than is permitted by apatite stoichiometry. In these cases, we determine a minimum Cl:F ratio by assuming $1 - X_{Cl} = X_F$. This adjustment in the measured F/Cl ratio is warranted because we did not observe variability in the chlorine X-ray count rates; however, estimation of a missing component is not possible for these analyses. By applying these methods, the detection limit of a missing component in F-rich apatite is 0.08 structural formulae units (McCubbin et al., 2010b); however, Jones et al. (2014) demonstrated that F-rich apatite with more than 0.08 sfu missing component can match measured OH abundances within about 0.02 sfu using the methods employed in this study. Equating a missing structural component to OH in Cl-rich apatite is more dubious because of the presence of structural vacancies and/or oxy-substitution on the apatite X-site (Hovis and Harlov, 2010; Schettler et al., 2011; Jones et al., 2014; McCubbin and Ustunisik, 2018). Although we compute a missing component in eucrite apatite, only quantitative measurements of OH in apatite are used to determine H_2O abundances in eucrites and in the bulk silicate portion of 4 Vesta.

The quality of apatite analyses is assessed based on stoichiometric constraints and electron microprobe totals. If analytical totals were outside of the range 97.0-102.0 wt.%, the analysis was discarded. The leniency on analytical total deficiency is due to the possibility of up to 1.79 wt.% H_2O (as OH- ions) in apatite, which cannot be detected by the electron microprobe. The REE abundances of eucrite apatite are much less than lunar apatite (Jolliff et al., 1993; McCubbin et al., 2011), so we do not expect highly deficient totals from missing REE. If the stoichiometry of the P

or Ca sites deviated by more than ±2% (i.e., 0.06 structural formula units (sfu) or 0.10 sfu on a 13-anion basis for the P- and Ca-sites, respectively), the analysis was discarded.

3.0 RESULTS

We report new data from apatite grains in the non-cumulate, unbrecciated eucrites CMS 04049, GRA 98098, LEW 88010, MAC 02522, MAC 041169, QUE 94484, and QUE 97053 (Table 2; Tables S2–S8). We also report new data from apatite grains in the monomict eucrite breccias Berthoud and Stannern (Table 2; Table S1; Table S9). These data are combined with previously published apatite data (Table S10) from five additional non-cumulate unbrecciated eucrites (i.e., Bates Nunataks (BTN) 00300, Elephant Moraine (EET) 90020, LEW 88009, Northwest Africa (NWA) 5073, and PCA 91078) and five additional monomict eucrite breccias (Cachari, EET 87542, Juvinas, Nuevo Laredo, and Padvarninkai). Although other studies report analyses of apatite within a broader set of eucrites than those considered here, we limited our study to basaltic unbrecciated or monomict breccias where the bulk rock composition is more likely to represent a melt composition. Consequently, we did not include apatite from polymict breccias or cumulate eucrites. In addition, we did not include residual eucrites, which have complex thermal histories that may have involved partial melt extraction (Yamaguchi et al., 2009). A complete list of all samples used in this study, their lithologic type and geochemical classification, and their average apatite F, Cl, and OH X-site compositions are provided in Table 1. All of the apatite analyses from this study are provided in the supplementary Tables S1–S9, and average apatite compositions from this study are reported in Table 2.

We determined the modal mineralogy within GRA 98098, MAC 041169, PCA 91078, QUE 97053, Stannern, and Berthoud. Our modal mineralogy estimates include a breakdown of the abundance of both merrillite and apatite in each sample, which allowed us to estimate the bulk

rock abundance of fluorine in these samples. The modal abundances and bulk rock fluorine contents are reported in Table 3.

3.1. Phosphate mineralogy and textural analysis of apatite in eucrites

All of the samples investigated in this study contain apatite, and apatite coexists with the volatile-free phosphate mineral merrillite, as noted in previous studies (e.g., Patiño Douce and Roden, 2006; Sarafian et al., 2013). The total abundance of phosphates in eucrites is typically <<1 vol%, and for the samples we analyzed, it was typically <0.25 vol% (Table 3). In addition, the ratio of apatite to merrillite varies from sample to sample with apatite as the dominant phosphate in GRA 98098, MAC 041169, PCA 91078, and Stannern and merrillite the dominant phosphate in Berthoud and QUE 97053 (Table 3). Apatite occurs in numerous textural occurrences, but it most commonly occurs as discrete subhedral grains that are within late-stage mesostasis, adjacent to other late-stage phases such as silica, troilite, merrillite, and various Fe-oxides (Figure 2c–d). Rare euhedral apatite also occurs in eucrites (Figure 2a). In metamorphosed eucrites that exhibit granoblastic textures, apatite is often included within pyroxene and plagioclase grains (Figure 2a–b). Apatite in eucrites exhibit a wide range of crystal sizes, from ~1 to >100 μm in the shortest dimension (Sarafian et al., 2013; Figure 2). Full section X-ray maps of GRA 98098, MAC 041169, PCA 91078, QUE 97053, Stannern, and three sections of Berthoud are provided in Figures 3 and 1, respectively. Corresponding full section BSE images are reported in Figures S1–S2.

3.2. F, Cl, OH, and S population of the X-site in eucrite apatite

Apatite in eucrites have chlorine abundances ranging from 0 to 17 mol% of the X-site, fluorine abundances ranging from 37 to ~100 mol% of the X-site, and missing component abundances ranging from 0 to 62 mol% of the X-site (Table 1; Tables S1–S10). Apatite in eucrites exhibit a substantial range in the F-OH portion of the F-Cl-OH apatite ternary, but they exhibit

very little variation in the Cl-component (Figure 4). Moreover, the abundances of F and OH can vary substantially within a single sample, but Cl abundances in most samples exhibit much less variation. Although some of the variation in F-OH observed in individual samples is real (based on quantitative SIMS measurements of H_2O), some of the variation may be attributable to the variation in F X-ray count rates, which is at least partly responsible for many analyses exhibiting apatite X-site sums that exceed one structural formula unit (Tables S1–S9). Sulfur may also contribute to excessive X-site sums. Based on the fO_2 of eucrites being between ΔIW-1 and ΔIW-2 (Stolper, 1977; Righter and Drake, 1996), any S in apatite should be present in the apatite structure as sulfide (Konecke et al., 2017, 2019; Brounce et al., 2019). Sulfide should occupy the apatite X-site (Pan and Fleet, 2002; Kim et al., 2017), so we have included S in our X-site sums; however, many of the apatite in eucrites are adjacent to troilite, and S and Fe abundances are often positively correlated in our analyses (Table 2; Tables S1–S9). Consequently, some of the S we measured in apatite may be coming from nearby troilite. A more detailed study of S in eucrite apatite is needed to characterize their contribution to eucrite apatite X-sites.

Apatite within eucrites are predominantly chlorine-poor fluorapatite that span a narrow range of F-Cl-OH ternary space (Figure 4) compared to basalts from other celestial bodies like Earth, Moon, and Mars (c.f., McCubbin et al., 2015a; Filiberto et al., 2016). The range in apatite X-site composition of eucrites is most similar to lunar mare basalts (McCubbin and Jones, 2015), but apatite in eucrites exhibit a narrower range of Cl abundances. Although we did not directly determine the H_2O abundances of apatite in the present study, previous studies have directly determined H_2O abundances in eucrite apatite by secondary ion mass spectrometry (SIMS). These data confirm that hydroxyl is the primary "missing" constituent of the X-site within eucrite apatite, similar to apatite in basalts from Earth, Moon, and Mars (e.g., Piccoli and Candela, 2002;

Greenwood et al., 2011; Barnes et al., 2020). Given the variation in F X-ray count rates for many of our analyses, we do not use our computed OH to make any estimates of H_2O in eucrite magmas or the eucrite source. Instead, we use published SIMS data that report measured H_2O abundances in apatite. The H_2O abundances of apatite in non-cumulate eucrites and monomict brecciated eucrites is in the range of 36–7183 ppm (Sarafian et al., 2013, 2014, 2017b; Barrett et al., 2016, 2021; Stephant et al., 2021). A complete tabulation of all apatite electron microprobe analyses from the present study are provided in the online supplementary data file (Tables S1–S9) along with the X-site occupancies of previously published eucrite apatite (Table S10). We report average apatite X-site compositions for each sample and those reported in earlier studies in Table 1, and we report average electron microprobe analyses of apatite from the present study in Table 2.

3.3. Bulk rock abundances of F in eucrites

Bulk rock abundances of F are needed to use apatite-based melt hygrometry and chlorometry (McCubbin et al., 2015b). Prior to this study, fluorine abundances were reported for 6 non-cumulate and/or monomict brecciated eucrites, and the values are in the range of 15–53 ppm F (Reed, 1964; Reed and Jovanovic, 1969; Wänke et al., 1972, 1977; Palme et al., 1978; Dreibus et al., 1979). The samples analyzed previously include Stannern, Nuevo Laredo, Juvinas, Béréba, Jonzac, and Haraiya. Of those samples, apatite X-site data are only available for Stannern, Nuevo Laredo, and Juvinas (Table S10). In this study, we report F abundances for GRA 98098, MAC 041169, PCA 91078, QUE 97053, Stannern, and Berthoud. The F abundances from the samples we analyzed are in the range of 7.6–54 ppm (Table 3). Our value for Stannern of 54 ± 5 ppm F is similar to that reported in the literature at 48 ppm F (Kitts and Lodders, 1998), lending further credence to our method of bulk rock F estimation. All of the samples for which bulk rock abundances of F were determined also have corresponding apatite compositions; consequently, we

have eight eucrites with sufficient data to apply apatite-based melt hygrometry and/or chlorometry methods.

We assessed the reproducibility of our modal abundance estimates by analyzing 3 different thin sections of Berthoud (Figure 1; Figure S1). We report the average modal mineralogy of Berthoud in Table 3 along with computed 1-sigma standard deviations. The modal abundance of apatite in the three sections of Berthoud are 0.044%, 0.035%, and 0.022%; however, the section with the lowest amount of apatite had an anomalously high amount of quenched impact melt (3.2 vol%; Figure 1b; Table S11) that likely contributed to the lower abundance of apatite in that sample given that apatite is one of the first phases to melt during partial melting. This range yields an average of 0.034% ± 0.009. Although additional work is needed to examine the reproducibility of apatite modal abundances by X-ray mapping techniques, we consider ~27% error to be a promising result for trace phases that make up less than 0.1% of the mineral mode.

4.0 DISCUSSION

4.1. Abundances of F, Cl, and H_2O in eucrite magmas from apatite

4.1.1. Abundance of F in eucrites

The concentrations of elements within a bulk rock provide an accurate reflection of the composition of the melt from which the rock crystallized as long as that rock is a representative sample of the melt. Crystal accumulation, fractional crystallization, assimilation of exogenous material, and degassing can all modify the pristine abundances of elements within a bulk rock sample. Magmatic volatiles are particularly susceptible to degassing during ascent or eruption onto the surface of a planetary body, but volatile-loss will ultimately occur even at depth as crystallization proceeds and volatile saturation is reached in the residual melt (e.g., Dixon et al., 1991; Carroll and Webster, 1994; Jambon, 1994; Dixon and Stolper, 1995; Holloway, 1998;

Webster et al., 1999; Aiuppa et al., 2009; Dasgupta and Dixon, 2009; Ustunisik et al., 2015). Fluorine is much less susceptible to degassing (Aiuppa et al., 2009; Ustunisik et al., 2015) in comparison to Cl and H, and this may be further aided by the high compatibility of F in apatite (McCubbin et al., 2015b). Consequently, bulk rock abundances of F are more likely to provide accurate reflections of F concentrations in parental melts compared to Cl or H, which remain incompatible during crystallization of F-rich apatite (Mathez and Webster, 2005; McCubbin et al., 2015b; Li and Hermann, 2017; McCubbin and Ustunisik, 2018).

4.1.2. Application of apatite-based melt hygrometry and chlorometry to eucrites

The bulk rock abundances of F in eucrites from previous studies and those determined here are in the range of 7.6–54 ppm (Table 4). These F bulk rock abundances are much higher than estimates based on F abundances in eucrite pyroxenes, which are in the range of 1.5–2.4 ppm (Sarafian et al., 2019). If the lower values of F reported by Sarafian et al. (2019) are more representative of eucrite melts, it implies that there is substantial apatite accumulation in eucrites to account for the higher bulk rock F abundances given that apatite is the primary mineralogical host for F in eucrites. However, apatite is not a cumulus phase in eucrites; it occurs as a trace phase in the late-stage mesostasis of eucrites. Consequently, we conclude that the bulk rock abundances of F determined on the basis of apatite modal abundances are more likely to reflect the F abundances of eucrite melts computed based on F abundances in pyroxene. The discrepancy between these two methods of estimation may indicate additional work is needed to understand the partitioning relationship of F between pyroxene and silicate melt under conditions that are similar to the crystallization conditions of eucrites.

Apatite is the only igneous mineral with F, Cl, and OH as essential structural constituents that has been identified and analyzed in eucrites. Although apatite is present in nearly all eucrites,

it typically occurs in only trace abundances (Sarafian et al., 2013; Table 3). The widespread occurrence of apatite in eucrites makes it an enticing sample set to apply apatite-based melt hygrometry and chlorometry because estimates for a wide range of samples can be determined using a single mineralogical tool. The required inputs for the apatite-based hygrometer/chlorometer include F, Cl, and H_2O abundances of apatite. From these inputs, Cl/F and H_2O/F abundance ratios of the melt are determined. These ratios can be used to compute bulk rock abundances of Cl and H_2O if bulk rock abundances of F are known. There are twelve eucrites for which bulk rock abundances of F have been determined (Table 4), including six from previous studies of eucrites (Dreibus et al., 1979; Kitts and Lodders, 1998; Mittlefehldt, 2015). Apatite compositions have been reported for eight of those twelve samples (Table S10). The eight samples with both bulk rock F and apatite compositions represent the basis for which the H_2O and Cl abundances of eucrite magmas are estimated (Table 4).

The use of apatite as a recorder of magmatic volatiles is not without complicating factors such as determining appropriate apatite-melt partitioning relationships for F, Cl, and H as well as accounting for processes that could have modified pristine volatile ratios in melt prior to being recorded in apatite (e.g., degassing, assimilation, or fractional crystallization; Boyce et al., 2014; McCubbin et al., 2016). Firstly, eucrite apatite exhibit X-site compositions (Sarafian et al., 2013, 2014; Figure 4) that are amenable to use of an apatite-based magmatic hygrometer and chlorometer that was developed for Fe-rich basaltic melt compositions at oxygen fugacities between IW and ΔIW-1, pressures from 0–1.2 GPa, and temperatures of 950–1050 °C (Boyce et al., 2014; McCubbin et al., 2015b; McCubbin and Ustunisik, 2018). These conditions are similar to the expected conditions under which eucrite apatite crystallized (Stolper, 1977; Righter and Drake, 1997). Secondly, F, Cl, and H_2O are all incompatible elements, so their ratios to each other in the

melt will remain largely unchanged during crystallization of nominally volatile-free minerals in a closed system. At the onset of apatite crystallization, the apatite will record the initial H_2O/F and Cl/F ratios of the parent melt if the system remained closed. However, changes to these ratios can occur during magmatic degassing or through assimilation of materials exogenous to the magmatic system. If magmatic degassing or assimilation occurs prior to the onset of apatite saturation, it is difficult, and many times impossible, to determine parent melt H_2O/F and Cl/F ratios from apatite. Apatite is a late-crystallizing phase, and it cannot record processes that occurred prior to apatite saturation, which is the primary limitation of using apatite to estimate Cl and H_2O abundances in parent magmas and magmatic source regions. To help mitigate this problem, we estimate Cl and H_2O abundances for an array of eucrites, which we compare to previous estimates of eucrite volatile abundances determined using apatite, nominally anhydrous minerals, and/or element ratios paired with geochemical relationships (Dreibus and Wänke, 1980; Sarafian et al., 2017b, 2019; McCubbin and Barnes, 2019; Stephant et al., 2021).

After the onset of apatite crystallization, degassing, assimilation, and/or fractional crystallization can cause changes in melt H_2O/F and Cl/F ratios that can result in intrasample variations in apatite X-site composition (Figure 5). Although assimilation can drive apatite compositions in any direction depending on the composition of the assimilated material, degassing and fractional crystallization each cause apatite compositions to evolve in somewhat predictable, yet opposite, directions (Boyce et al., 2014; McCubbin et al., 2016; Figure 5). Apatite crystallization during degassing will cause apatite compositions to evolve towards fluorapatite given that both H and Cl are more susceptible to degassing than F (Aiuppa et al., 2009; Ustunisik et al., 2015). In contrast, apatite crystallization during fractional crystallization will cause apatite compositions to evolve away from fluorapatite (Boyce et al., 2014; McCubbin et al., 2016; Figure

5). In samples with Cl-poor apatite, like eucrites, mare basalts, and many terrestrial basalts (McCubbin and Jones, 2015; Figure 4), the apatite evolutionary paths for degassing and fractional crystallization converge, but they evolve in opposite directions (Figure 5). In samples with intrasample variations in apatite X-site composition, the earliest formed apatite will yield the initial H_2O/F and Cl/F ratios of the parent melt if the system remained closed prior to apatite saturation. Most of the eucrites exhibit intrasample variation in apatite X-site composition, and that variation is consistent with either fractional crystallization or magmatic degassing (Figures 4–5). If the variation in apatite X-site compositions is caused by degassing, the most accurate estimate of Cl/F and H_2O/F parent melt ratios would be derived from the most Cl-rich and H_2O-rich apatite. In contrast, if the variation in apatite X-site compositions is caused by fractional crystallization, the most accurate estimate of parent melt volatile composition would come from the most Cl- and H_2O-poor apatite. Ideally, we would have a dataset where F, Cl, and H_2O are determined on the same apatite grains to determine how Cl and H_2O are correlated, but the number of SIMS analyses of H_2O in eucrite apatite is highly limited, and many datasets do not report F, Cl, and H_2O on the same apatite grains, preventing such an analysis. Furthermore, we cannot definitively distinguish whether the intrasample variation of apatite in each sample is the result of degassing or fractional crystallization because, as discussed earlier, Cl-poor systems yield very similar apatite X-site distributions in a given sample for both degassing and fractional crystallization, albeit with opposite evolutionary paths as crystallization proceeds (Figure 5). Moreover, textural analysis of apatite within the eucrites yielded ambiguous results as to the relative timing of apatite crystallization within each sample. Consequently, we compute Cl/F and H_2O/F melt ratios based on average apatite compositions in each eucrite sample, which yields less precise results that more

accurately reflect the Cl/F and H_2O/F ratios in eucrite melts than any individual apatite measurement in a sample (Table 4).

4.1.3. Abundance of H_2O in eucrites

Based on the apatite-melt exchange coefficients reported by McCubbin et al. (2015b), average apatite F abundances in Table S10, and SIMS measurements of H_2O in apatite from Stannern, Juvinas, PCA 91078, Padvarninkai, Cachari, and EET 90020 (Table 4), the eucrites have H_2O/F melt ratios of 1.1–5.3 with an average H_2O/F melt ratio of 2.5 ± 1.5. Although there are also H_2O data acquired by SIMS for GRA 98098, the data exhibit substantial variation in H_2O abundances that resulted in uncertainties in melt H_2O/F ratio of ≥100%, so it was excluded from the mean. Of the samples with reasonable uncertainties in melt H_2O/F ratio, Stannern, Juvinas, and PCA 91078 have known bulk rock abundances of F (Table S10) that indicate parent melt H_2O abundances of 160 ± 110 ppm, 50 ± 35 ppm, and 31 ± 6 ppm, respectively. Our computed melt concentrations of H_2O using apatite-based melt hygrometry are similar to estimates determined from water abundances in eucrite pyroxenes of 50–116 ppm H_2O (Sarafian et al., 2019; Stephant et al., 2021). The general agreement between estimates using nominally anhydrous minerals and apatite indicates that both methods may yield robust estimates of H_2O abundances in planetary samples. For apatite, this notion is further supported by recent studies that have demonstrated the ability of apatite to preserve primary signatures of H after shock events caused by impacts (e.g., Černok et al., 2020).

4.1.4. Abundance of Cl in eucrites

The apatite-melt exchange coefficients reported by McCubbin et al. (2015b) coupled with the composition of apatite in eucrites indicate that eucrites have Cl/F melt ratios of 0.02–1.4. Furthermore, the eucrites have an average Cl/F melt ratio of 0.21 ± 0.11 on the basis of F and Cl

abundances in apatite from all the samples used in this study with the exception of EET 90020, MAC 02522, and GRA 98098 (Table 4). For EET 90020, many of the apatite had Cl abundances at or below analytical detection for the electron microprobe, so we excluded that sample from the mean. For MAC 02522, only two apatite grains were measured, and they exhibit substantial variation in Cl abundances that resulted in uncertainties in melt Cl/F ratio of ≥100%, so it was excluded from the mean. GRA 98098 was also excluded from the mean because it is a distinct outlier compared to all of the other samples with a melt Cl/F estimate of 1.4 (i.e., the other samples yielded melt Cl/F ratios of 0.08–0.44). It is possible that GRA 98098 apatite formed from a Cl-rich melt or fluid that is quite dissimilar to the parent melts of the other eucrites studied, but regardless of the origin of this high Cl/F signature, GRA 98098 is clearly an outlier (e.g., Figure 4) and as such can be excluded from the mean. Of the samples with estimated melt Cl/F ratios, Stannern, Nuevo Laredo, Juvinas, GRA 98098, MAC 041169, QUE 97053, Berthoud, and PCA 91078 have known bulk rock abundances of F (Table S10) that indicate parent melt Cl abundances of 11 ± 2 ppm, 14 ± 4 ppm, 2.0 ± 0.6 ppm, 52 ± 10 ppm, 3.5 ± 0.9 ppm, 3.4 ± 0.7 ppm, 2.5 ± 0.4 ppm, and 2 ± 1 ppm, respectively.

4.2. Abundances of F, Cl, and H_2O in 4 Vesta

4.2.1. Previous estimates of F, Cl, and H_2O in 4 Vesta

Several studies have reported abundances of F and/or H_2O in 4 Vesta (Dreibus and Wänke, 1980; McCubbin and Barnes, 2019; Sarafian et al., 2019; Stephant et al., 2021), and one study has reported the abundance of Cl in 4 Vesta (Dreibus and Wänke, 1980). Dreibus and Wänke (1980) used a limited number of bulk rock measurements of F and Cl and volatile/refractory element ratios to determine that the bulk silicate portion of 4 Vesta (BSV) has 4.6 ppm Cl and 4.8 ppm F. Sarafian et al. (2019) used F and H_2O measurements of Mg-rich cores of eucrite pyroxene and considered

the two leading hypotheses on eucrite petrogenesis (i.e., serial magmatism or melt extracts from a magma ocean) to report two possible ranges of F and H_2O abundances in BSV. Their first estimate considered a model where eucrites formed by 20–30% partial melting of their source and yielded 0.3–0.7 ppm F and 10–21 ppm H_2O in BSV. Their second model assumed eucrites were extracted after 20–80% crystallization of a magma ocean and yielded 0.3–2 ppm F and 10–70 ppm H_2O in BSV. Stephant et al. (2021) also used H_2O measurements of Mg-rich cores of eucrite pyroxene to estimate that the bulk silicate portion of 4 Vesta has 12–23 ppm H_2O, assuming that eucrites formed as melt extracts after 80-85% magma ocean crystallization. McCubbin and Barnes (2019) used apatite-based melt hygrometry and volatile/refractory element ratios to determine that 4 Vesta has 13–25 ppm H_2O in BSV, which overlaps with estimates of H_2O using nominally anhydrous minerals. To further evaluate the range of F, Cl, and H_2O in 4 Vesta, we use apatite-based melt hygrometry on a larger subset of samples than has been used in previous studies.

4.2.2. Method for computing F, Cl, and H_2O abundances in 4 Vesta from apatite

There are two primary methods that can be used to estimate the abundances of F, Cl, and H_2O in 4 Vesta. The first uses knowledge of eucrite petrogenesis to back out source abundances from parental melt compositions. This method is similar to the one applied to 4 Vesta by Sarafian et al. (2019) and that has also been used previously to determine abundances of volatiles in the Moon and Mars (McCubbin et al., 2015a, 2016). This method is not ideal for application to 4 Vesta because there are two competing models for eucrite petrogenesis—the serial magmatism model and the magma ocean crystallization model—that would each yield different abundance estimates of F, Cl, and H_2O. Moreover, this method requires making assumptions about the degree of partial melting or percentage of magma ocean crystallization before melt extraction to determine F, Cl,

and H_2O abundances. All of these factors complicate the application of this method, so we do not consider it further.

The second method to estimate the abundances of F, Cl, and H_2O in 4 Vesta is agnostic to eucrite petrogenesis and relies on the ratio of fluorine to a similarly incompatible refractory element (i.e., Nd or Dy) along with Cl/F and H_2O/F ratios from apatite-based melt chlorometry and hygrometry, respectively. Fluorine is paired with Nd or Dy because both are refractory lithophile elements, and their abundances can be estimated from models of the bulk composition of 4 Vesta. Furthermore, Nd, Dy, and F are similarly incompatible during igneous differentiation processes over a wide range of geological conditions (Saal et al., 2002; Chen et al., 2015; Ni et al., 2019). Using the estimated abundance of F in 4 Vesta, the abundance of Cl and H_2O can be computed from the Cl/F and H_2O/F ratios from apatite-based melt chlorometry and hygrometry, respectively. The practice of using elemental ratios has provided important insights into the composition of the bulk silicate portions of Earth, Moon, Mars, and 4 Vesta (Dreibus and Wänke, 1980, 1985; Schilling et al., 1980; Hofmann and White, 1983; McDonough and Sun, 1995; Taylor, 2013; Albarède et al., 2015; Hauri et al., 2015; Lin and van Westrenen, 2019). We use this method to estimate F, Cl, and H_2O abundances in the bulk silicate portion of 4 Vesta.

Before we can determine F abundances in BSV, we need to determine the abundances of Dy and Nd in BSV. The values used by Dreibus and Wänke (1980) to determine the bulk composition of 4 Vesta assume an enrichment in REE relative to CI by a factor of 2.5, which is much higher than the enrichment factor for other refractory lithophile elements in their model like Ti (2.18), Ca (2.04), and Sc (2.10), implying super-chondritic enrichments in REE relative to other refractory elements in their 4 Vesta bulk composition. Furthermore, Dreibus and Wänke (1980) estimated that the core size of 4 Vesta represents at least 20% of its mass, but data returned from

the DAWN spacecraft indicate a slightly smaller core mass fraction of 18% (Russell et al., 2012), which should represent an upper limit to the core mass fraction of primordial 4 Vesta given that collisional erosion through time would preferentially remove the silicate portions of 4 Vesta. Consequently, we reevaluated abundances of Dy and Nd in 4 Vesta.

Hundreds of additional HED meteorites have been discovered in the 40 years following the seminal publication of Dreibus and Wänke (1980), and the DAWN spacecraft has yielded additional information that have enabled updated models for the bulk composition of 4 Vesta (e.g., Toplis et al., 2013). The favored model for the bulk composition of 4 Vesta from Toplis et al. (2013) constitutes 75% of an H chondrite-like component and 25% of a CM chondrite-like component. This composition optimized numerous mineralogical, petrological, and geochemical constraints, but it is not a perfect match on the basis of the depletions in ^{48}Ca, ^{50}Ti, and ^{54}Cr in HED meteorites compared to all known chondrites (Trinquier et al., 2007, 2009; Leya et al., 2008; Schiller et al., 2018). Nonetheless, refractory element abundances in HED meteorites exhibit chondritic ratios (Mittlefehldt, 2015), so we use the 75%H–25%CM model to determine the abundances of Dy and Nd in the bulk silicate portion of 4 Vesta. Based on the compositions of H chondrites, dehydrated/decarbonated CM chondrites, degree of alkali depletion on 4 Vesta relative to CI chondrite, and the core mass fraction of 0.18 for 4 Vesta (Wasson and Kallemeyn, 1988; Righter and Drake, 1997; Russell et al., 2012; Kumler and Day, 2021), we estimate Dy and Nd abundances in BSV of 0.473 ppm Dy and 0.877 ppm Nd. Our estimate indicates that Dy and Nd are enriched relative to CI chondrite by a factor of ~1.9, which is considerably lower than earlier estimates (Dreibus and Wänke, 1980; Ruzicka et al., 1997).

4.2.3. Abundance of F in 4 Vesta

The eucrites have F/Nd and F/Dy melt ratios of 2.9–9.6 and 5.4–18.4, respectively and average F/Nd and F/Dy ratios of 5.8 ± 2.4 and 10.9 ± 4.2, respectively (Table S12). These values were determined on the basis of bulk rock abundances of F, Nd, and Dy in Stannern, Nuevo Laredo, Juvinas, Béréba, Jonzac, Haraiya, and GRA 98098 (Kitts and Lodders, 1998; Warren et al., 2009; Mittlefehldt, 2015; Table S12). Based on the Nd (0.877 ppm) and Dy (0.473 ppm) abundances in BSV, we estimate an F abundance of 3.0–7.2 ppm (Table 4). This value is within error of the F abundance reported by Dreibus and Wänke, (1980) at 4.8 ppm F, and it is higher than the estimate from Sarafian et al. (2019) at 0.3–2 ppm F.

4.2.4. Abundance of H_2O in 4 Vesta

The computed abundance of F in the bulk silicate portion of 4 Vesta was combined with the H_2O/F ratios determined from apatite-based melt hygrometry to estimate an H_2O abundance in BSV of 3.6–22 ppm (Table 4). This value agrees well with previous estimates that used apatite-based melt hygrometry (McCubbin and Barnes, 2019), and it agrees well with the pyroxene-based H_2O estimates that assumed eucrites formed by serial magmatism (i.e., 10–21 ppm H_2O; Sarafian et al., 2019). Our estimates also agree with the far low end of the pyroxene-based H_2O estimate that assumed eucrites are melt extracts from a magma ocean (i.e., 10–70 ppm H_2O; Sarafian et al., 2019; Stephant et al., 2021). The far low end of the estimates corresponds to eucrite extraction after about 70–85% crystallization of the magma ocean, which is similar to the model of Mandler and Elkins-Tanton (2013) that called for 60–70% crystallization of 4 Vesta's magma ocean before eucrite extraction.

4.2.5. Abundance of Cl in 4 Vesta and the peculiarity of GRA 98098

The computed abundance of F in the bulk silicate portion of 4 Vesta was combined with the Cl/F ratios determined from apatite-based melt chlorometry to estimate a Cl abundance in BSV

of 0.39–1.8 ppm (Table 4). This value is depleted relative to the estimate of 4.6 ppm Cl from Dreibus and Wänke, (1980) and indicates that Cl is more depleted in 4 Vesta than reported previously. This estimate excluded sample GRA 98098 because it has a Cl/F ratio >1, making it a clear outlier compared to the other eucrites. On the basis of only GRA 98098, it implies a Cl content in 4 Vesta of 6.9 ppm Cl. Previous studies have pointed out the Cl-rich nature of GRA 98098 and have hinted that it may preserve a "Vestan KREEP component", analogous to lunar KREEP (Sarafian et al., 2013, 2017b; Barrett et al., 2019). Much like the lunar KREEP reservoir (Boyce et al., 2015; Barnes et al., 2016b, 2019; McCubbin and Barnes, 2020), apatite in GRA 98098 record both elevated Cl/F and elevated δ^{37}Cl values (Sarafian et al., 2017b). However, the other incompatible trace element abundances in GRA 98098 do not corroborate a "KREEPy" origin (Warren et al., 2009). Even if degassing can explain the elevated δ^{37}Cl values in GRA 98098, degassing would have lowered the Cl/F ratio of the bulk rock from its initial value, and the present Cl/F ratio of the bulk rock is already anomalously high. The anomalous Cl/F and Cl isotopic composition of apatite in GRA 98098 may be representative of its source, which would indicate Cl/F and Cl isotopic heterogeneities in the interior of 4 Vesta. Alternatively, GRA 98098 could have interacted with a Cl-rich, incompatible trace element-poor, crustal fluid that had elevated δ^{37}Cl. The origin of elevated Cl/F and elevated δ^{37}Cl in GRA 98098 apatite remains unknown, but additional eucrites with similarly high Cl/F ratios are needed before we can determine the importance of GRA 98098 to understanding eucrite petrogenesis.

4.3. Implications for the origin of volatile depletion on 4 Vesta

One of the earliest observations of HED meteorites was their pervasive depletion in moderately volatile and highly volatile elements compared to CI chondrites (Dreibus et al., 1977; McSween et al., 2011). The moderately volatile elements (MVE) K and Na are depleted in the

bulk silicate portion of 4 Vesta by ~0.1 × CI (Dreibus and Wänke, 1980; Righter and Drake, 1997), which is similar to the degree of alkali depletion in the bulk silicate portion of the Moon (Taylor and Wieczorek, 2014). Other MVE such as Zn, Rb, Cs, and Pb also show depletions in the silicate portion of 4 Vesta that are similar to the bulk silicate portion of the Moon (Kumler and Day, 2021), although some of these elements could have been depleted through core formation processes, particularly if 4 Vesta has an S-rich core (Steenstra et al., 2019, 2020). In addition to volatile abundances, volatile element stable isotopic compositions of eucrites also indicate volatile depletion through enrichments of heavier isotopes compared to the isotopic ratios recorded by chondrites (Paniello et al., 2012; Sarafian et al., 2017b; Barrett et al., 2019; Tian et al., 2019). The origin and timing of volatile depletion on 4 Vesta is less constrained, but the low $^{87}Sr/^{86}Sr$ and high $^{206,207}Pb/^{204}Pb$ in eucrites indicate volatile depletion on 4 Vesta occurred early (Moynier et al., 2012; Hans et al., 2013; Day and Moynier, 2014; Kumler and Day, 2021), through some combination of the accretion of volatile-depleted building blocks and very early loss from the parent body (e.g., degassing of a magma ocean and/or core formation).

4.3.1. F and Cl depletion in 4 Vesta

In the present study, we constrained the abundances of the moderately volatile elements F and Cl, and the highly volatile element H in the bulk silicate portion of 4 Vesta. The abundance of F in the bulk silicate portion of 4 Vesta is depleted by 0.08–0.1 × CI, which is similar to other MVE depletions in 4 Vesta (e.g., Na, K, Zn, Rb, Cs, and Pb; Dreibus and Wänke, 1980; Kumler and Day, 2021). Moreover, the F abundance estimated for BSV is within error of the bulk F abundance in the bulk silicate portion of the Moon (Hauri et al., 2015; McCubbin et al., 2015a), corroborating evidence that both are depleted in moderately volatile elements to a similar degree.

In contrast to F, the abundance of Cl in the bulk silicate portion of 4 Vesta is depleted by 0.00056–0.0027 × CI, which is highly depleted relative to other MVE in 4 Vesta. The Moon and Earth also record relatively extreme depletion in Cl compared to other MVE with similar 50% condensation temperatures (Sharp and Draper, 2013; Boyce et al., 2018), but the degree of depletion is more pronounced on 4 Vesta and similar to basalts derived from partial melting of mantle compositions from which a primary crust had been previously extracted (Figure 6), which would be inconsistent with both competing models for eucrite petrogenesis (i.e., the serial magmatism model and the magma ocean crystallization model). The consistent depletion in Cl relative to CI chondrites in differentiated bodies have led some to infer that the 50% condensation temperature at 10^{-4} bar for Cl (i.e., 948 K; Lodders, 2003) is overestimated and that Cl behaves more like a highly volatile element (Zolotov and Mironenko, 2007; Sharp et al., 2016; Wood et al., 2019). The consistent depletion of Cl in differentiated parent bodies has also been ascribed to overestimated abundances of Cl in CI chondrites (Clay et al., 2017), although this conclusion has been called into question (Palme and Zipfel, 2021). Additional work is needed to evaluate both possibilities, but the origin of Cl depletion in 4 Vesta may provide important clues as to the process(es) by which 4 Vesta became depleted in volatiles.

4.3.2. Implications for Cl on the origin of volatile depletion in 4 Vesta

The depletion of Cl in the Earth and Moon has been attributed to collisional erosion and magma ocean degassing, respectively (Sharp and Draper, 2013; Boyce et al., 2015). Eucrites display a large variation in δ^{37}Cl values (Sarafian et al., 2017b; Barrett et al., 2019, 2021), albeit less extreme than those recorded in lunar samples (Sharp et al., 2010; Tartèse et al., 2014; Boyce et al., 2015; Barnes et al., 2016b, 2019; Potts et al., 2018; Wang et al., 2019; McCubbin and Barnes, 2020). These elevated δ^{37}Cl values in eucrite apatite have been interpreted as indicating magma

ocean degassing of Cl on 4 Vesta (Sarafian et al., 2017b). However, δ^{37}Cl values in lunar samples are positively correlated with incompatible trace element abundances (Boyce et al., 2015; Barnes et al., 2016b, 2019), demonstrating a link between magma ocean crystallization (i.e., increases in incompatible trace element abundances in residual magma ocean melt) and degassing of metal chlorides (i.e., increases in δ^{37}Cl values). In contrast, the eucrites seem to show an opposite trend with δ^{37}Cl values that are anti-correlated with incompatible trace elements (Barrett et al., 2019; Figure 7). Although the La/Yb–δ^{37}Cl systematics are consistent with the presence of Cl-isotopic heterogeneities within the interior of 4 Vesta, these heterogeneities cannot be explained solely by degassing of a global magma ocean.

The Cl isotopic heterogeneities recorded in eucrite apatite may reflect heterogeneities in the eucrite source region(s), or they could arise through secondary processes such as late-stage magmatic degassing and/or metamorphism (Barrett et al., 2019; Kumler and Day, 2021). If the eucrites arise from an initially homogenous source with the same Cl/F ratio (as would be expected for a partial melt extract from a global magma ocean that had not reached apatite saturation), secondary heating processes or late-stage magmatic degassing should result in a negative correlation between bulk rock Cl/F ratios and δ^{37}Cl values given that (1) isotopic fractionation would be driven by the loss of a volatile species favoring ^{35}Cl (e.g. metal chlorides), and (2) Cl is much more susceptible to degassing relative to F (Aiuppa et al., 2009; Ustunisik et al., 2015). However, eucrites do not exhibit variations in δ^{37}Cl that are negatively correlated with Cl/F ratio (Figure 8). In fact, the most ^{37}Cl-rich and ^{37}Cl-poor samples have the two highest Cl/F ratios (Figure 8). Moreover, the apatite exhibit large variations in δ^{37}Cl values even over a comparatively narrow range of Cl/F ratios (Figure 8). Consequently, the Cl/F–δ^{37}Cl systematics of eucrites cannot be explained solely by late-stage magmatic degassing or volatile loss through thermal

metamorphism. Consequently, we interpret the range in $\delta^{37}Cl$ values in eucrites as an indication of a Vestan mantle that has a heterogeneous Cl-isotopic composition that likely preserves the Cl-isotopic heterogeneity and volatile depletion of its building blocks. In fact, Cl-isotopic heterogeneities are present even in chondrite meteorites (Sharp et al., 2013b), and thermal processing of 4 Vesta's precursor materials prior to inheritance would have only aided the loss of volatiles and broadened the range of $\delta^{37}Cl$ values beyond those recorded in chondrites. This interpretation strongly favors the serial magmatism model for the origin of eucrites because a global magma ocean should have largely erased any Cl isotopic and Cl/F heterogeneities inherited by the mantle from its precursor materials. Although such heterogeneities can be preserved even during large-scale melting of the parent body (i.e., sufficient for core formation), the preservation of Cl isotopic and Cl/F heterogeneities in the eucrite source poses problems for any model that invokes a homogenous, parent-body wide magma ocean once existed on 4 Vesta. Alternatively, if the Vestan crust hosts both ^{37}Cl-rich and ^{37}Cl-poor fluid sources, the extreme $\delta^{37}Cl$ values recorded in GRA 98098 and NWA 5073 could be explained, respectively, without having strong implications for eucrite petrogenesis. However, these fluids could not account for the observed anticorrelation between bulk rock La/Yb ratios and $\delta^{37}Cl$ values in eucrites (Figure 7) or the overall depletion of moderately volatile elements, particularly the extreme depletion in Cl (Figure 6). Additional data on the Cl/F–$\delta^{37}Cl$–La/Yb systematics of a broader range of eucrite samples is needed to better characterize the extent and origin of volatile-element heterogeneities in the interior of 4 Vesta.

4.3.3. H_2O depletion in 4 Vesta

The abundance of H_2O in the bulk silicate portion of 4 Vesta is depleted by 0.000026–0.00016 × CI, which is highly depleted relative to less volatile components in 4 Vesta. The H_2O

abundance of the bulk silicate portion of the Moon is poorly constrained compared to 4 Vesta and is in the range of 3.1–84 ppm H_2O (McCubbin et al., 2015a; Ni et al., 2019), which encompasses the estimated range for BSV at 3.6–22 ppm H_2O (Table 4). These results indicate that 4 Vesta is depleted in some highly volatile elements to a similar degree as the Moon, consistent with the degree of depletion in moderately volatile elements, exclusive of Cl.

The H-isotopic composition of 4 Vesta has been determined, and δD values range from –292‰ to +163‰ for the analyses that have 2σ uncertainties below 90‰ (Sarafian et al., 2014, 2017b; Barrett et al., 2016, 2021; Stephant et al., 2021). The range in H isotopic compositions for the entire suite of eucrites is similar to the intrasample variation in δD recorded in individual samples, indicating that the source(s) for eucrites may have a fairly homogenous H-isotopic composition; however, additional data, particularly for diogenites, are needed to fully characterize the H-isotopic composition of the Vestan interior.

5.0 CONCLUSIONS

The asteroid 4 Vesta is a protoplanet with a degree of volatile depletion in moderately and highly volatile elements, exclusive of Cl, that is similar to the Moon. This depletion in volatile elements is likely inherited, at least in part, from the precursor materials that accreted to form 4 Vesta and is unlikely to result solely from degassing of a global magma ocean. We used a combination of apatite-based melt hygrometry/chlorometry and appropriately paired volatile/refractory element ratios to determine that the bulk silicate portion of 4 Vesta has 3.0–7.2 ppm F, 0.39–1.8 ppm Cl, and 3.6–22 ppm H_2O. The Cl/F ratios of eucrites coupled with their Cl-isotopic compositions indicate that they likely formed through serial magmatism of a source with heterogeneous $\delta^{37}Cl$ and Cl/F rather than by melt extraction from a partially crystallized global magma ocean. The serial magmatism model has also been favored in a recent study on the basis

of incompatible trace element compositions in eucrites (Kumler and Day, 2021). Although our results can be reconciled with the past presence of a partial magma ocean on 4 Vesta, any model for eucrite petrogenesis involving a global magma ocean must be able to account for the preservation of a heterogeneous eucrite source with respect to Cl/F ratios and Cl isotopes.

6.0 ACKNOWLEDGEMENTS

We are grateful to the Meteorite Working Group, now the Antarctic Meteorite Review Panel of the Astromaterials Allocation Review Board, for carefully evaluating our sample requests, and we thank the curatorial staff at NASA Johnson Space Center for allocation of the Antarctic eucrites used in this study. The US Antarctic meteorite samples are recovered by the Antarctic Search for Meteorites (ANSMET) program which has been funded by NSF and NASA and characterized and curated by the Department of Mineral Sciences of the Smithsonian Institution and Astromaterials Acquisition and Curation Office at NASA Johnson Space Center, respectively. We also thank Carl Agee of the Institute of Meteoritics at the University of New Mexico in Albuquerque, NM, USA for the allocation of Berthoud, and we thank Ludovic Ferrière of the Naturhistorisches (Natural History) Museum in Vienna, Austria for the allocation of Stannern. Finally, we wish to thank Daniel Kent Ross for his help with using the electron microprobe at NASA JSC and working closely with F.M.M., J.A.L., J.J.B., and J.W.B. to implement our apatite analytical routines. Kent will be dearly missed, and we dedicate this work to his memory. We are grateful to Wim van Westrenen for the editorial handling of this manuscript and to Thomas Barrett and an anonymous reviewer that provided constructive and helpful comments that improved the overall quality of this work. F.M.M. and J.W.B. were supported by NASA's Planetary Science Research Program during this work. J.A.L. was supported by the NASA Postdoctoral Program

during this work. J.J.B was supported by start-up funds from the University of Arizona. S.M.E. acknowledges support from NASA Solar System Workings grant 80NSSC19K0752.

7.0 REFERENCES

Aiuppa A., Baker D. R., and Webster J. D. (2009) Halogens in volcanic systems. *Chem. Geol.* **263**, 1-18.

Albarède F. (2009) Volatile accretion history of the terrestrial planets and dynamic implications. *Nature* **461**, 1227-1233.

Albarède F., Albalat E., and Lee C. T. A. (2015) An intrinsic volatility scale relevant to the Earth and Moon and the status of water in the Moon. *Meteorit. Planet. Sci.* **50**, 568-577.

Albarède F., Ballhaus C., Blichert-Toft J., Lee C. T., Marty B., Moynier F., and Yin Q. Z. (2013) Asteroidal impacts and the origin of terrestrial and lunar volatiles. *Icarus* **222**, 44-52.

Alexander C. M. O. D., McKeegan K. D., and Altwegg K. (2018) Water Reservoirs in Small Planetary Bodies: Meteorites, Asteroids, and Comets. *Space Sci. Rev.* **214**. DOI: 10.1007/s11214-018-0474-9

Barnes J. J., Kring D. A., Tartèse R., Franchi I. A., Anand M., and Russell S. S. (2016a) An asteroidal origin for water in the Moon. *Nat. Comm.* **7**. DOI: 10.1038/ncomms11684

Barnes J. J., Tartèse R., Anand M., McCubbin F. M., Neal C. R., and Franchi I. A. (2016b) Early degassing of lunar urKREEP by crust-breaching impact(s). *Earth Planet. Sci. Lett.* **447**, 84-94.

Barnes J. J., Franchi I. A., McCubbin F. M., and Anand M. (2019) Multiple volatile reservoirs on the Moon revealed by the isotopic composition of chlorine in lunar basalts. *Geochim. Cosmochim. Acta* **266**, 144-162.

Barnes J. J., McCubbin F. M., Santos A. R., Day J. M. D., Boyce J. W., Schwenzer S. P., Ott U., Franchi I. A., Messenger S., Anand M., and Agee C. B. (2020) Multiple early-formed water reservoirs in the interior of Mars. *Nat. Geosci.* **13**, 260-264.

Barrett T. J., Barnes J. J., Tartèse R., Anand M., Franchi I. A., Greenwood R. C., Charlier B. L. A., and Grady M. M. (2016) The abundance and isotopic composition of water in eucrites. *Meteorit. Planet. Sci.* **51**, 1110-1124.

Barrett T. J., Barnes J. J., Anand M., Franchi I. A., Greenwood R. C., Charlier B. L. A., Zhao X., Moynier F., and Grady M. M. (2019) Investigating magmatic processes in the early Solar System using the Cl isotopic systematics of eucrites. *Geochim. Cosmochim. Acta* **266**, 582-597.

Barrett T. J., Černok A., Degli-Alessandrini G., Zhao X., Anand M., Franchi I. A., and Darling J. R. (2021) Exploring relationships between shock-induced microstructures and H_2O and Cl in apatite grains from eucrite meteorites. *Geochim. Cosmochim. Acta* **302**, 120-140.

Beck A. W., Lawrence D. J., Peplowski P. N., Prettyman T. H., McCoy T. J., McSween H. Y., Jr., Toplis M. J., and Yamashita N. (2015) Using HED meteorites to interpret neutron and gamma-ray data from asteroid 4 Vesta. *Meteorit. Planet. Sci.* **50**, 1311-1337.

Binzel R. P. and Xu S. (1993) Chips off of Asteroid 4 Vesta: Evidence for the parent body of basaltic achondrite meteorites. *Science* **260**, 186-191.

Boss A. P. (1998) Temperatures in protoplanetary disks. *Ann. Rev. Earth Planet. Sci.* **26**, 53-80.

Bottke W. F., Nesvorny D., Grimm R. E., Morbidelli A., and O'Brien D. P. (2006) Iron meteorites as remnants of planetesimals formed in the terrestrial planet region. *Nature* **439**, 821-824.

Bouvier A., Blichert-Toft J., Boyet M., and Albarède F. (2015) ^{147}Sm-^{143}Nd and ^{176}Lu-^{176}Hf systematics of eucrite and angrite meteorites. *Meteorit. Planet. Sci.* **50**, 1896-1911.

Boyce J. W., Liu Y., Rossman G. R., Guan Y., Eiler J. M., Stolper E. M., and Taylor L. A. (2010) Lunar apatite with terrestrial volatile abundances. *Nature* **466**, 466-469.

Boyce J. W., Tomlinson S. M., McCubbin F. M., Greenwood J. P., and Treiman A. H. (2014) The Lunar Apatite Paradox. *Science* **344**, 400-402.

Boyce J. W., Treiman A. H., Guan Y., Ma C., Eiler J. M., Gross J., Greenwood J. P., and Stolper E. M. (2015) The chlorine isotope fingerprint of the lunar magma ocean. *Sci. Adv.* **1**. DOI: 10.1126/sciadv.1500380

Boyce J. W., Kanee S. A., McCubbin F. M., Barnes J. J., Bricker H., and Treiman A. H. (2018) Early loss, fractionation, and redistribution of chlorine in the Moon as revealed by the low-Ti lunar mare basalt suite. *Earth Planet. Sci. Lett.* **500**, 205-214.

Boynton W. V., Taylor G. J., Evans L. G., Reedy R. C., Starr R., Janes D. M., Kerry K. E., Drake D. M., Kim K. J., Williams R. M. S., Crombie M. K., Dohm J. M., Baker V., Metzger A. E., Karunatillake S., Keller J. M., Newsom H. E., Arnold J. R., Bruckner J., Englert P. A. J., Gasnault O., Sprague A. L., Mitrofanov I., Squyres S. W., Trombka J. I., d'Uston L., Wanke H., and Hamara D. K. (2007) Concentration of H, Si, Cl, K, Fe, and Th in the low- and mid-latitude regions of Mars. *J. Geophys. Res. Planet.* **112**. DOI: 10.1029/2007JE002887

Brounce M., Boyce J., McCubbin F. M., Humphreys J., Reppart J., Stolper E., and Eiler J. (2019) The oxidation state of sulfur in lunar apatite. *Am. Min.* **104**, 307-312.

Burbine T. H., Buchanan P. C., Binzel R. P., Bus S. J., Hiroi T., Hinrichs J. L., Meibom A., and McCoy T. J. (2001) Vesta, vestoids, and the howardite, eucrite, diogenite group: Relationships and the origin of spectral differences. *Meteorit. Planet. Sci.* **36**, 761-781.

Campbell I. H. and Taylor S. R. (1983) No water, no granites - No oceans, no continents. *Geophys. Res. Lett.* **10**, 1061-1064.

Canup R. M., Visscher C., Salmon J., and Fegley B., Jr. (2015) Lunar volatile depletion due to incomplete accretion within an impact-generated disk. *Nat. Geosci.* **8**, 918-921.

Carroll M. R. and Webster J. D. (1994) Solubilities of sulfur, noble-gases, nitrogen, chlorine, and fluorine in magmas. *Rev. Min.* **30**, 231-279.

Černok A., Anand M., Zhao X. C., Darling J. R., White L. F., Stephant A., Dunlop J., Tait K. T., and Franchi, I. A., (2020) Preservation of primordial signatures of water in highly-shocked ancient lunar rocks. *Earth Planet. Sci. Lett.* **544**. DOI: 10.1016/j.epsl.2020.116364

Chambers, J. E. (2004) Planetary accretion in the inner Solar System. *Earth Planet. Sci. Lett.* **223**, 241-252.

Chen Y., Zhang Y. X., Liu Y., Guan Y. B., Eiler J., and Stolper E. M. (2015) Water, fluorine, and sulfur concentrations in the lunar mantle. *Earth Planet. Sci. Lett.* **427**, 37-46.

Chi, H., Dasgupta, R., Duncan, M. S. and Shimizu, N. (2014) Partitioning of carbon between Fe-rich alloy melt and silicate melt in a magma ocean – Implications for the abundance and origin of volatiles in Earth, Mars, and the Moon. *Geochim. Cosmochim. Acta* **139**, 447-471.

Clay P. L., Burgess R., Busemann H., Ruzié-Hamilton L., Joachim B., Day J. M. D., and Ballentine C. J. (2017) Halogens in chondritic meteorites and terrestrial accretion. *Nature* **551**, 614-618.

Connelly J. N., Bizzarro M., Krot A. N., Nordlund A., Wielandt D., and Ivanova M. A. (2012) The absolute chronology and thermal processing of solids in the solar protoplanetary disk. *Science* **338**, 651-655.

Dasgupta R. and Dixon J. E. (2009) Volatiles and volatile-bearing melts in the Earth's interior. *Chem. Geol.* **262**, 1-3.

Day J. M. D. and Moynier F. (2014) Evaporative fractionation of volatile stable isotopes and their bearing on the origin of the Moon. *Philos. Trans. Roy. Soc. Lond. A: Math. Phys. Eng. Sci.* **372**. DOI: 10.1098/rsta.2013.0259

Dixon J. E., Clague D. A., and Stolper E. M. (1991) Degassing history of water, sulfur, and carbon in submarine lavas from Kilauea Volcano, Hawaii. *J. Geol.* **99**, 371-394.

Dixon J. E. and Stolper E. M. (1995) An experimental study of water and carbon dioxide solubilities in mid-ocean ridge basaltic liquids. Part II: Applications to degassing. *J. Pet.* **36**, 1633-1646.

Drake M. J. (2005) Origin of water in the terrestrial planets. *Meteorit. Planet. Sci.* **40**, 519-527.

Dreibus G. and Wänke H. (1980) The bulk composition of the eucrite parent asteroid and its bearing on planetary evolution. *Zeitschrift Fur Naturforschung* **35**, 204-216.

Dreibus G. and Wänke H. (1985) Mars, a volatile-rich planet. *Meteoritics* **20**, 367-381.

Dreibus G., Kruse H., Spettel B., and Wänke H. (1977) The bulk composition of the Moon and eucrite parent body, *Proceedings of the 8th Lunar Science Conference*. Lunar and Planetary Institute, Houston, TX, **8**, 211-227.

Dreibus G., Spettel B., and Wänke H. (1979) Halogens in meteorites and their primordial abundances. *Phys. Chem. Earth* **11**, 33-38.

Ehlmann B. L., Anderson F. S., Andrews-Hanna J., Catling D. C., Christensen P. R., Cohen B. A., Dressing C. D., Edwards C. S., Elkins-Tanton L. T., Farley K. A., Fassett C. I., Fischer W. W., Fraeman A. A., Golombek M. P., Hamilton V. E., Hayes A. G., Herd C. D. K., Horgan B., Hu R., Jakosky B. M., Johnson J. R., Kasting J. F., Kerber L., Kinch K. M., Kite E. S., Knutson H. A., Lunine J. I., Mahaffy P. R., Mangold N., McCubbin F. M., Mustard J. F., Niles P. B., Quantin-Nataf C., Rice M. S., Stack K. M., Stevenson D. J., Stewart S. T., Toplis M. J., Usui T., Weiss B. P., Werner S. C., Wordsworth R. D., Wray J. J., Yingst R. A., Yung Y. L., and Zahnle K. J. (2016) The sustainability of habitability on terrestrial planets: Insights, questions, and needed measurements from Mars for understanding the evolution of Earth-like worlds. *J. Geophys. Res. Planet.* **121**, 1927-1961.

Evans L. G., Peplowski P. N., McCubbin F. M., McCoy T. J., Nittler L. R., Zolotov M. Y., Ebel D. S., Lawrence D. J., Starr R. D., Weider S. Z., and Solomon S. C. (2015) Chlorine on the surface of Mercury: MESSENGER gamma-ray measurements and implications for the planet's formation and evolution. *Icarus* **257**, 417-427.

Filiberto, J., Baratoux, D., Beaty, D., Breuer, D., Farcy, B. J., Grott, M., Jones, J. H., Kiefer, W. S., Mane, P., McCubbin, F. M. and Schwenzer, S. P. (2016) A review of volatiles in the Martian interior. *Meteorit. Planet. Sci.* **51**, 1935-1958.

Fowler G. W., Shearer C. K., Papike J. J., and Layne G. D. (1995) Diogenites as asteroidal cumulates: Insights from orthopyroxene trace element chemistry. *Geochim. Cosmochim. Acta* **59**, 3071-3084.

Gaetani G. A. and Grove T. L. (1998) The influence of water on melting of mantle peridotite. *Contrib. Min. Pet.* **131**, 323-346.

Gillis J. J., Jolliff B. L., and Korotev R. L. (2004) Lunar surface geochemistry: Global concentrations of Th, K, and FeO as derived from lunar prospector and Clementine data. *Geochim. Cosmochim. Acta* **68**, 3791-3805.

Greenwood J. P., Itoh S., Sakamoto N., Warren P., Taylor L., and Yurimoto H. (2011) Hydrogen isotope ratios in lunar rocks indicate delivery of cometary water to the Moon. *Nat. Geosci.* **4**, 79-82.

Greenwood R. C., Franchi I. A., Jambon A., Buchanan P. C. (2005) Widespread magma oceans on asteroidal bodies in the early Solar System. *Nature* **435**, 916-918.

Hans U., Kleine T., and Bourdon B. (2013) Rb-Sr chronology of volatile depletion in differentiated protoplanets: BABI, ADOR and ALL revisited. *Earth Planet. Sci. Lett.* **374**, 204-214.

Hauri E. H., Weinreich T., Saal A. E., Rutherford M. C., and Van Orman J. A. (2011) High pre-eruptive water contents preserved in lunar melt inclusions. *Science* **333**, 213-215.

Hauri E. H., Saal A. E., Rutherford M. J., and Van Orman J. A. (2015) Water in the Moon's interior: Truth and consequences. *Earth Planet. Sci. Lett.* **409**, 252-264.

Hirth G. and Kohlstedt D. L. (1996) Water in the oceanic upper mantle: Implications for rheology, melt extraction and the evolution of the lithosphere. *Earth Planet. Sci. Lett.* **144**, 93-108.

Hofmann A. W. and White W. M. (1983) Ba, Rb and Cs in the Earth's mantle. *Zeitschrift Fur Naturforschung* **38**, 256-266.

Holloway J. R. (1998) Graphite-melt equilibria during mantle melting: Constraints on CO_2 in MORB magmas and the carbon content of the mantle. *Chem. Geol.* **147**, 89-97.

Hopkins M. D., Mojzsis S. J., Bottke W. F., and Abramov O. (2015) Micrometer-scale U-Pb age domains in eucrite zircons, impact re-setting, and the thermal history of the HED parent body. *Icarus* **245**, 367-378.

Hovis, G. L. and Harlov, D. E. (2010) Solution calorimetric investigation of fluor-chlorapatite crystalline solutions. *Am. Min.* **95**, 946-952.

Hublet G., Debaille V., Wimpenny J., and Yin Q. Z. (2017) Differentiation and magmatic activity in Vesta evidenced by ^{26}Al-^{26}Mg dating in eucrites and diogenites. *Geochim. Cosmochim. Acta* **218**, 73-97.

Jambon A. (1994) Earth degassing and large-scale geochemical cycling of volatile elements. *Rev. Min.* **30**, 479-517.

Jarosewich E. and Boatner L. A. (1991) Rare-earth element reference samples for electron microprobe analysis. *Geostandards Newsletter* **15**, 397-399.

Jarosewich E., Nelen J. A., and Norberg J. A. (1980) Reference samples for electron microprobe analysis. *Geostandards Newsletter* **4**, 43-47.

Jolliff B. L., Haskin L. A., Colson R. O., and Wadhwa M. (1993) Partitioning in REE-saturating minerals - theory, experiment, and modeling of whitlockite, apatite, and evolution of lunar residual magmas. *Geochim. Cosmochim. Acta* **57**, 4069-4094.

Jones, R. H., McCubbin, F. M., Dreeland, L., Guan, Y. B., Burger, P. V. and Shearer, C. K. (2014) Phosphate minerals in LL chondrites: A record of the action of fluids during metamorphism on ordinary chondrite parent bodies. *Geochim. Cosmochim. Acta* **132**, 120-140.

Kim Y., Konecke B., Fiege A., Simon A., and Becker U. (2017) An ab-initio study of the energetics and geometry of sulfide, sulfite, and sulfate incorporation into apatite: The thermodynamic basis for using this system as an oxybarometer. *Am. Min.* **102**, 1646-1656.

Kitts K. and Lodders K. (1998) Survey and evaluation of eucrite bulk compositions. *Meteorit. Planet. Sci.* **33**, A197-A213.

Kleine T., Touboul M., Bourdon B., Nimmo F., Mezger K., Palme H., Jacobsen S. B., Yin Q.-Z., and Halliday A. N. (2009) Hf-W chronology of the accretion and early evolution of asteroids and terrestrial planets. *Geochim. Cosmochim. Acta* **73**, 5150-5188.

Konecke B. A., Fiege A., Simon A. C., Parat F., and Stechern A. (2017) Co-variability of S^{6+}, S^{4+}, and S^{2-} in apatite as a function of oxidation state: Implications for a new oxybarometer. *Am. Min.* **102**, 548-557.

Konecke B. A., Fiege A., Simon A. C., Linsler S., and Holtz F. (2019) An experimental calibration of a sulfur-in-apatite oxybarometer for mafic systems. *Geochim. Cosmochim. Acta* **265**, 242-258.

Kumler B. and Day J. M. D. (2021) Trace element variations generated by magmatic and post-crystallization processes in eucrite meteorites. *Geochim. Cosmochim. Acta* **301**, 211-229.

Lawrence D. J., Puetter R. C., Elphic R. C., Feldman W. C., Hagerty J. J., Prettyman T. H., and Spudis P. D. (2007) Global spatial deconvolution of Lunar Prospector Th abundances. *Geophys. Res. Lett.* **34**. DOI: 10.1029/2006GL028530

Lewis J. A. and Jones R. H. (2016) Phosphate and feldspar mineralogy of equilibrated L chondrites: The record of metasomatism during metamorphism in ordinary chondrite parent bodies. *Meteorit. Planet. Sci.* **51**, 1886-1913.

Leya I., Schönbächler M., Wiechert U., Krähenbühl U., and Halliday A. N. (2008) Titanium isotopes and the radial heterogeneity of the solar system. *Earth Planet. Sci. Lett.* **266**, 233-244.

Li H. J. and Hermann J. (2017) Chlorine and fluorine partitioning between apatite and sediment melt at 2.5 GPa, 800 ^{o}C: A new experimentally derived thermodynamic model. *Am. Min.* **102**, 580-594.

Lin, Y. and van Westrenen, W. (2019) Isotopic evidence for volatile replenishment of the Moon during the Late Accretion. *Natl. Sci. Rev.* **6**, 1247-1254.

Lodders K. (2003) Solar system abundances and condensation temperatures of the elements. *Astrophys. J.* **591**, 1220-1247.

Lodders K. and Fegley B. (1998) The Planetary Scientist's Companion. Oxford University Press, New York.

Lugmair G. W. and Shukolyukov A. (1998) Early solar system timescales according to ^{53}Mn-^{53}Cr systematics. *Geochim. Cosmochim. Acta* **62**, 2863-2886.

Mandler B. E. and Elkins-Tanton L. T. (2013) The origin of eucrites, diogenites, and olivine diogenites: Magma ocean crystallization and shallow magma chamber processes on Vesta. *Meteorit. Planet. Sci.* **48**, 2333-2349.

Marty B. (2012) The origins and concentrations of water, carbon, nitrogen and noble gases on Earth. *Earth Planet. Sci. Lett.* **313**, 56-66.

Mason H. E., McCubbin F. M., Smirnov A., and Phillips B. L. (2009) Solid-state NMR and IR spectroscopic investigation of the role of structural water and F in carbonate-rich fluorapatite. *Am. Min.* **94**, 507-516.

Mathez E. A. and Webster J. D. (2005) Partitioning behavior of chlorine and fluorine in the system apatite-silicate melt-fluid. *Geochim. Cosmochim. Acta* **69**, 1275-1286.

McCord T. B., Johnson T. V., and Adams J. B. (1970) Asteroid Vesta: Spectral reflectivity and compositional implications. *Science* **168**, 1445-1447.

McCubbin F. M. and Barnes J. J. (2019) Origin and abundances of H_2O in the terrestrial planets, Moon, and asteroids. *Earth Planet. Sci. Lett.* **526**. DOI: 10.1016/j.epsl.2019.115771

McCubbin F. M. and Barnes J. J. (2020) The chlorine-isotopic composition of lunar KREEP from magnesian-suite troctolite 76535. *Am. Min.* **105**, 1270-1274.

McCubbin F. M. and Jones R. H. (2015) Extraterrestrial apatite: Planetary geochemistry to astrobiology. *Elements* **11**, 183-188.

McCubbin F. M. and Ustunisik G. (2018) Experimental investigation of F and Cl partitioning between apatite and Fe-rich basaltic melt at 0 GPa and 950-1050 ºC: Evidence for steric controls on apatite-melt exchange equilibria in OH-poor apatite. *Am. Min.* **103**, 1455-1467.

McCubbin F. M., Steele A., Hauri E. H., Nekvasil H., Yamashita S., and Hemley R. J. (2010a) Nominally hydrous magmatism on the Moon. *Proc. Nat. Acad. Sci.* **27**, 11223-11228.

McCubbin F. M., Steele A., Nekvasil H., Schnieders A., Rose T., Fries M., Carpenter P. K., and Jolliff B. L. (2010b) Detection of structurally bound hydroxyl in fluorapatite from Apollo mare basalt 15058,128 using TOF-SIMS. *Am. Min.* **95**, 1141-1150.

McCubbin F. M., Jolliff B. L., Nekvasil H., Carpenter P. K., Zeigler R. A., Steele A., Elardo S. M., and Lindsley D. H. (2011) Fluorine and chlorine abundances in lunar apatite: Implications for heterogeneous distributions of magmatic volatiles in the lunar interior. *Geochim. Cosmochim. Acta* **75**, 5073-5093.

McCubbin F. M., Hauri E. H., Elardo S. M., Vander Kaaden K. E., Wang J., and Shearer C. K. (2012) Hydrous melting of the martian mantle produced both depleted and enriched shergottites. *Geology* **40**, 683-686.

McCubbin F. M., Vander Kaaden K. E., Tartèse R., Klima R. L., Liu Y., Mortimer J., Barnes J. J., Shearer C. K., Treiman A. H., Lawrence D. J., Elardo S. M., Hurley D. M., Boyce J. W., and Anand M. (2015a). Magmatic volatiles (H, C, N, F, S, Cl) in the lunar mantle, crust, and regolith: Abundances, distributions, processes, and reservoirs. *Am. Min.* **100**, 1668-1707.

McCubbin F. M., Vander Kaaden K. E., Tartèse R., Boyce J. W., Mikhail S., Whitson E. S., Bell A. S., Anand M., Franchi I. A., Wang J. H., and Hauri E. H. (2015b) Experimental investigation of F, Cl, and OH partitioning between apatite and Fe-rich basaltic melt at 1.0-1.2 GPa and 950-1000 ºC. *Am. Min.* **100**, 1790-1802.

McCubbin F. M., Boyce J. W., Srinivasan P., Santos A. R., Elardo S. M., Filiberto J., Steele A., and Shearer C. K. (2016) Heterogeneous distribution of H_2O in the martian interior: Implications for the abundance of H_2O in depleted and enriched mantle sources. *Meteorit. Planet. Sci.* **51**, 2036-2060.

McCubbin F. M., Phillips B. L., Adcock C. T., Tait K. T., Steele A., Vaughn J. S., Fries M. D., Atudorei V., Vander Kaaden K. E., and Hausrath E. M. (2018) Discreditation of bobdownsite and the establishment of criteria for the identification of minerals with essential monofluorophosphate (PO_3F^{2-}). *Am. Min.* **103**, 1319-1328.

McDonough W. F. and Sun S. S. (1995) The composition of the Earth. *Chem. Geol.* **120**, 223-253.

McSween H. Y., Jr., Mittlefehldt D. W., Beck A. W., Mayne R. G., and McCoy T. J. (2011) HED meteorites and their relationship to the geology of Vesta and the Dawn Mission. *Space Sci. Rev.* **163**, 141-174.

McSween H. Y., Jr., Binzel R. P., De Sanctis M. C., Ammannito E., Prettyman T. H., Beck A. W., Reddy V., Le Corre L., Gaffey M. J., McCord T. B., Raymond C. A., Russell C. T., and Dawn Sci. T. (2013) Dawn; the Vesta-HED connection; and the geologic context for eucrites, diogenites, and howardites. *Meteorit. Planet. Sci.* **48**, 2090-2104.

Misawa K., Yamaguchi A., and Kaiden H. (2005) U-Pb and ^{207}Pb-^{206}Pb ages of zircons from basaltic eucrites: Implications for early basaltic volcanism on the eucrite parent body. *Geochim. Cosmochim. Acta* **69**, 5847-5861.

Mittlefehldt D. W. (2015) Asteroid (4) Vesta: I. The howardite-eucrite-diogenite (HED) clan of meteorites. *Chem. Der Erde* **75**, 155-183.

Moynier F., Paniello R. C., Gounelle M., Albarède F., Beck P., Podosek F., and Zanda B. (2011) Nature of volatile depletion and genetic relationships in enstatite chondrites and aubrites inferred from Zn isotopes. *Geochim. Cosmochim. Acta* **75**, 297-307.

Moynier F., Day J. M. D., Okui W., Yokoyama T., Bouvier A., Walker R. J., and Podosek F. A. (2012) Planetary-scale strontium isotopic heterogeneity and the age of volatile depletion of early Solar system materials. *Astrophys. J.* **758**. DOI: 10.1088/0004-637X/758/1/45

Nakajima M. and Stevenson D. J. (2018) Inefficient volatile loss from the Moon-forming disk: Reconciling the giant impact hypothesis and a wet Moon. *Earth Planet. Sci. Lett.* **487**, 117-126.

Ni, P., Zhang, Y. and Guan, Y. (2017) Volatile loss during homogenization of lunar melt inclusions. *Earth Planet. Sci. Lett.* **478**, 214-224.

Ni P., Zhang Y., Chen S., and Gagnon J. (2019) A melt inclusion study on volatile abundances in the lunar mantle. *Geochim. Cosmochim. Acta* **249**, 17-41.

Norris C. A. and Wood B. J. (2017) Earth's volatile contents established by melting and vaporization. *Nature* **549**, 507-510.

O'Brien D. P., Izidoro A., Jacobson S. A., Raymond S. N., and Rubie D. C. (2018) The delivery of water during terrestrial planet formation. *Space Sci. Rev.* **214**. DOI: 10.1007/s11214-018-0475-8

Palme H. (2000) Are there chemical gradients in the inner solar system? *Space Sci. Rev.* **92**, 237-262.

Palme H. and Zipfel J. (2021) The composition of CI chondrites and their contents of chlorine and bromine: Results from instrumental neutron activation analysis. *Meteorit. Planet. Sci.* DOI: 10.1111/maps.13720

Palme H., Baddenhausen H., Blum K., Cendales M., Dreibus G., Hofmeister H., Kruse H., Palme C., Spettel B., Vilcsek E., and Wänke H. (1978) New data on lunar samples and achondrites and a comparison of the least fractionated samples from the Earth, the Moon, and the eucrite parent body, *Proceedings of the 9th Lunar and Planetary Science Conference*. Lunar and Planetary Institute, Houston, TX, **9**, 25-57.

Pan Y. M. and Fleet M. E. (2002) Compositions of the apatite-group minerals: Substitution mechanisms and controlling factors. *Rev. Min. Geochem.* **48**, 13-49.

Paniello R. C., Moynier F., Beck P., Barrat J.-A., Podosek F. A., and Pichat S. (2012) Zinc isotopes in HEDs: Clues to the formation of 4-Vesta, and the unique composition of Pecora Escarpment 82502 *Geochim. Cosmochim. Acta* **86**, 76-87.

Patiño Douce A. E. and Roden M. F. (2006) Apatite as a probe of halogen and water fugacities in the terrestrial planets. *Geochim. Cosmochim. Acta* **70**, 3173-3196.

Persikov E. S., Zharikov V. A., Bukhtiyarov P. G., and Polskoy S. F. (1990) The effect of volatiles on the properties of magmatic melts. *Euro. J. Min.* **2**, 621-642.

Piccoli P. M. and Candela P. A. (2002) Apatite in igneous systems. *Rev. Min. Geochem.* **48**, 255-292.

Potts N. J., Barnes J. J., Tartèse R., Franchi I. A., and Anand M. (2018) Chlorine isotopic compositions of apatite in Apollo 14 rocks: Evidence for widespread vapor-phase

metasomatism on the lunar nearside similar to 4 billion years ago. *Geochim. Cosmochim. Acta* **230**, 46-59.

Potts, P. J. and Tindle, A. G. (1989) Analytical characteristics of a multilayer dispersion element (2d = 60 Å) in the determination of fluorine in minerals by electron microprobe. *Min. Mag.* **53**, 357-362.

Preibisch S., Saalfeld S., and Tomancak P. (2009) Globally optimal stitching of tiled 3D microscopic image acquisitions. *Bioinformatics* **25**, 1463-1465.

Prettyman T. H., Hagerty J. J., Elphic R. C., Feldman W. C., Lawrence D. J., McKinney G. W., and Vaniman D. T. (2006) Elemental composition of the lunar surface: Analysis of gamma ray spectroscopy data from Lunar Prospector. *J. Geophys. Res. Planets* **111**. DOI: 10.1029/2005JE002656

Prettyman T. H., Yamashita N., Reedy R. C., McSween H. Y., Jr., Mittlefehldt D. W., Hendricks J. S., and Toplis M. J. (2015) Concentrations of potassium and thorium within Vesta's regolith. *Icarus* **259**, 39-52.

Pringle E. A., Savage P. S., Badro J., Barrat J.-A., and Moynier F. (2013) Redox state during core formation on asteroid 4-Vesta. *Earth Planet. Sci. Lett.* **373**, 75-82.

Raymond S. N., Quinn T., and Lunine J. I. (2004) Making other earths: dynamical simulations of terrestrial planet formation and water delivery. *Icarus* **168**, 1-17.

Reed G. W. (1964) Fluorine in stone meteorites. *Geochim. Cosmochim. Acta* **28**, 1729-1743.

Reed G. W. and Jovanovic S. (1969) Some halogen measurements on achondrites. *Earth Planet. Sci. Lett.* **6**, 316-320.

Righter, K. (2019) Volatile element depletion of the Moon—The roles of precursors, post-impact disk dynamics, and core formation. *Sci. Adv.* **5**, DOI: 10.1126/sciadv.aau7658.

Righter K. and Drake M. J. (1996) Core formation in Earth's Moon, Mars, and Vesta. *Icarus* **124**, 513-529.

Righter K. and Drake M. J. (1997) A magma ocean on Vesta: Core formation and petrogenesis of eucrites and diogenites. *Meteorit. Planet. Sci.* **32**, 929-944.

Roszjar J., Metzler K., Bischoff A., Barrat J.-A., Geisler T., Greenwood R. C., Franchi I. A., and Klemme S. (2011) Thermal history of Northwest Africa 5073—A coarse-grained Stannern-trend eucrite containing cm-sized pyroxenes and large zircon grains. *Meteorit. Planet. Sci.* **46**, 1754-1773.

Russell C. T., Raymond C. A., Coradini A., McSween H. Y., Zuber M. T., Nathues A., De Sanctis M. C., Jaumann R., Konopliv A. S., Preusker F., Asmar S. W., Park R. S., Gaskell R., Keller H. U., Mottola S., Roatsch T., Scully J. E. C., Smith D. E., Tricarico P., Toplis M. J., Christensen U. R., Feldman W. C., Lawrence D. J., McCoy T. J., Prettyman T. H., Reedy R. C., Sykes M. E., and Titus T. N. (2012) Dawn at Vesta: Testing the protoplanetary paradigm. *Science* **336**, 684-686.

Ruzicka A., Snyder G. A., and Taylor L. A. (1997) Vesta as the howardite, eucrite and diogenite parent body: Implications for the size of a core and for large-scale differentiation. *Meteorit. Planet. Sci.* **32**, 825-840.

Saal A. E., Hauri E. H., Langmuir C. H., and Perfit M. R. (2002) Vapour undersaturation in primitive mid-ocean-ridge basalt and the volatile content of Earth's upper mantle. *Nature* **419**, 451-455.

Saal A. E., Hauri E. H., Lo Cascio M., Van Orman J. A., Rutherford M. C., and Cooper R. F. (2008) Volatile content of lunar volcanic glasses and the presence of water in the Moon's interior. *Nature* **454**, 192-195.

Salters V. J. M. and Stracke A. (2004) Composition of the depleted mantle. *Geochem. Geophys. Geosys.* **5**. DOI: 10.1029/2003GC000597

Sarafian A. R., Roden M. F., and Patiño Douce A. E. (2013) The volatile content of Vesta: Clues from apatite in eucrites. *Meteorit. Planet. Sci.* **48**, 2135-2154.

Sarafian A. R., Nielsen S. G., Marschall H. R., McCubbin F. M., and Monteleone B. D. (2014) Early accretion of water in the inner solar system from a carbonaceous chondrite-like source. *Science* **346**, 623-626.

Sarafian A. R., John T., Roszjar J., and Whitehouse M. J. (2017a) Chlorine and hydrogen degassing in Vesta's magma ocean. *Earth Planet. Sci. Lett.* **459**, 311-319.

Sarafian A. R., Hauri E. H., McCubbin F. M., Lapen T. J., Berger E. L., Nielsen S. G., Marschall H. R., Gaetani G. A., Righter K., and Sarafian E. (2017b) Early accretion of water and volatile elements to the inner Solar System: evidence from angrites. *Philos. Trans. Roy. Soc. Lond. A: Math. Phys. Eng. Sci.* **375**. DOI:10.1098/rsta.2016.0209

Sarafian A. R., Nielsen S. G., Marschall H. R., Hauri E. H., Gaetani G. A., Righter K., and Berger E. L. (2019) The water and Fluorine content of 4 Vesta. *Geochim. Cosmochim. Acta* **266**, 568-581.

Schettler, G., Gottschalk, M. and Harlov, D. E. (2011) A new semi-micro wet chemical method for apatite analysis and its application to the crystal chemistry of fluorapatite-chlorapatite solid solutions. *Am. Min.* **96**, 138-152.

Schiller M., Bizzarro M., and Fernandes V. A. (2018) Isotopic evolution of the protoplanetary disk and the building blocks of Earth and the Moon. *Nature* **555**, 507-510.

Schilling J. G., Bergeron M. B., and Evans R. (1980) Halogens in the mantle beneath the north-Atlantic. *Philos. Trans. Roy. Soc. Lond. A: Math. Phys. Eng. Sci.* **297**, 147-178.

Sharp Z. D. (2017) Nebular ingassing as a source of volatiles to the Terrestrial planets. *Chem. Geol.* **448**, 137-150.

Sharp Z. D. and Draper D. S. (2013) The chlorine abundance of Earth: Implications for a habitable planet. *Earth Planet. Sci. Lett.* **369-370**, 71-77.

Sharp Z. D., Helffrich G. R., Bohlen S. R., and Essene E. J. (1989) The stability of sodalite in the system $NaAlSiO_4$-NaCl. *Geochim. Cosmochim. Acta* **53**, 1943-1954.

Sharp Z. D., Shearer C. K., McKeegan K. D., Barnes J. D., and Wang Y. Q. (2010) The chlorine isotope composition of the Moon and implications for an anhydrous mantle. *Science* **329**, 1050-1053.

Sharp Z. D., McCubbin F. M., and Shearer C. K. (2013a) A hydrogen-based oxidation mechanism relevant to planetary formation. *Earth Planet. Sci. Lett.* **380**, 88-97.

Sharp Z. D., Mercer J. A., Jones R. H., Brearley A. J., Selverstone J., Bekker A., and Stachel T. (2013b) The chlorine isotope composition of chondrites and Earth. *Geochim. Cosmochim. Acta* **107**, 189-204.

Sharp Z. D., Williams J., Shearer C., Agee C., and McKeegan K. (2016) The chlorine isotope composition of Martian meteorites 2. Implications for the early solar system and the formation of Mars. *Meteorit. Planet. Sci.* **51**, 2111-2126.

Shearer C. K., Burger P., and Papike J. J. (2010) Petrogenetic relationships between diogenites and olivine diogenites: Implications for magmatism on the HED parent body. *Geochim. Cosmochim. Acta* **74**, 4865-4880.

Srinivasan G., Whitehouse M. J., Weber I., and Yamaguchi A. (2007) The crystallization age of eucrite zircon. *Science* **317**, 345-347.

Steenstra, E. S., Knibbe, J. S., Rai, N. and van Westrenen, W. (2016) Constraints on core formation in Vesta from metal–silicate partitioning of siderophile elements. *Geochim. Cosmochim. Acta* **177**, 48-61.

Steenstra, E. S., Dankers, D., Berndt, J., Klemme, S., Matveev, S. and van Westrenen, W. (2019) Significant depletion of volatile elements in the mantle of asteroid Vesta due to core formation. Icarus **317**, 669-681.

Steenstra, E. S., Berndt, J., Klemme, S., Rohrbach, A., Bullock, E. S. and van Westrenen, W. (2020) An experimental assessment of the potential of sulfide saturation of the source regions of eucrites and angrites: Implications for asteroidal models of core formation, late accretion and volatile element depletions. *Geochim. Cosmochim. Acta* **269**, 39-62.

Stephant, A., Wadhwa, M., Hervig, R., Bose, M., Zhao, X., Barrett, T.J., Anand, M. and Franchi, I.A. (2021) A deuterium-poor water reservoir in the asteroid 4 Vesta and the inner solar system. *Geochim. Cosmochim. Acta* **297**, 203-219.

Stolper E. (1977) Experimental petrology of eucritic meteorites. *Geochim. Cosmochim. Acta* **41**, 587-611.

Stormer J. C., Pierson M. L., and Tacker R. C. (1993) Variation of F-X-ray and Cl-X-ray intensity due to anisotropic diffusion in apatite during electron-microprobe analysis. *Am. Min.* **78**, 641-648.

Sutton S., Alexander C. M. O. D., Bryant A., Lanzirotti A., Newville M., and Cloutis E. A. (2017) The bulk valence state of Fe and the origin of water in chondrites. *Geochim. Cosmochim. Acta* **211**, 115-132.

Tang H. and Dauphas N. (2012) Abundance, distribution, and origin of ^{60}Fe in the solar protoplanetary disk. *Earth Planet. Sci. Lett.* **359**, 248-263.

Tartèse R., Anand M., Joy K. H., and Franchi I. A. (2014) H and Cl isotope systematics of apatite in brecciated lunar meteorites Northwest Africa 4472, Northwest Africa 773, Sayh al Uhaymir 169, and Kalahari 009. *Meteorit. Planet. Sci.* **49**, 2266-2289.

Taylor G. J. (2013) The bulk composition of Mars. *Chem. Der Erde* **73**, 401-420.

Taylor G. J. and Wieczorek M. A. (2014) Lunar bulk chemical composition: a post-gravity recovery and interior laboratory reassessment. *Philos. Trans. Roy. Soc. Lond. A: Math. Phys. Eng. Sci.* **372**. DOI: 10.1098/rsta.2013.0242

Tian Z., Chen H., Fegley B., Lodders K., Barrat J.-A., Day J. M. D., and Wang K. (2019) Potassium isotopic compositions of howardite-eucrite-diogenite meteorites. *Geochim. Cosmochim. Acta* **266**, 611-632.

Toplis M. J., Mizzon H., Monnereau M., Forni O., McSween H. Y., Mittlefehldt D. W., McCoy T. J., Prettyman T. H., De Sanctis M. C., Raymond C. A., and Russell C. T. (2013) Chondritic models of 4 Vesta: Implications for geochemical and geophysical properties. *Meteorit. Planet. Sci.* **48**, 2300-2315.

Touboul M., Sprung P., Aciego S. M., Bourdon B., and Kleine T. (2015) Hf-W chronology of the eucrite parent body. *Geochim. Cosmochim. Acta* **156**, 106-121.

Trinquier A., Birck J.-L., and Allegre C. J. (2007) Widespread ^{54}Cr heterogeneity in the inner solar system. *Astrophys. J.* **655**, 1179-1185.

Trinquier A., Birck J. L., Allegre C. J., Gopel C., and Ulfbeck D. (2008) ^{53}Mn-^{53}Cr systematics of the early Solar System revisited. *Geochim. Cosmochim. Acta* **72**, 5146-5163.

Trinquier A., Elliott T., Ulfbeck D., Coath C., Krot A. N., and Bizzarro M. (2009) Origin of nucleosynthetic isotope heterogeneity in the solar protoplanetary disk. *Science* **324**, 374-376.

Ustunisik G., Nekvasil H., Lindsley D. H., and McCubbin F. M. (2015) Degassing pathways of Cl-, F-, H-, and S-bearing magmas near the lunar surface: Implications for the composition and Cl isotopic values of lunar apatite. *Am. Min.* **100**, 1717-1727.

Wang Y., Hsu W., and Guan Y. (2019) An extremely heavy chlorine reservoir in the Moon: Insights from the apatite in lunar meteorites. *Sci. Rep.* **9**. DOI: 10.1038/s41598-019-42224-8

Wänke H., Baddenhausen H., Balacescu A., Teschke F., Spettel B., Dreibus G., Palme H., Quijano-Rico M., Kruse H., Wlotzka F., and Begemann F. (1972) Multielement analyses of lunar samples and some implications of the results, *Proceedings of the third lunar science conference*. M.I.T. Press, Houston, TX, **3**, 1251-1268.

Wänke H., Baddenhausen H., Blum K., Cendales M., Dreibus G., Hofmeister H., Kruse H., Jagoutz E., Palme C., Spettel B., Thacker R., and Vilcsek E. (1977) On the chemistry of lunar samples and achondrites. Primary matter in the lunar highlands: A re-evaluation, *Proceedings of the 8th lunar science conference*. Lunar and Planetary Institute, Houston, TX, **8**, 2191-2213.

Ward D., Bischoff A., Roszjar J., Berndt J., and Whitehouse M. J. (2017) Trace element inventory of meteoritic Ca-phosphates. *Am. Min.* **102**, 1856-1880.

Warren P. H. (1997) Magnesium oxide iron oxide mass balance constraints and a more detailed model for the relationship between eucrites and diogenites. *Meteorit. Planet. Sci.* **32**, 945-963.

Warren, P.H., Kallemeyn, G.W., Huber, H., Ulff-Møller, F. and Choe, W. (2009) Siderophile and other geochemical constraints on mixing relationships among HED-meteoritic breccias. *Geochim. Cosmochim. Acta* **73**, 5918-5943.

Wasson J. T. and Kallemeyn G. W. (1988) Compositions of chondrites. *Philos. Trans. Roy. Soc. Lond. A: Math. Phys. Eng. Sci.* **325**, 535-544.

Webster J. D. (2004) The exsolution of magmatic hydrosaline chloride liquids. *Chem. Geol.* **210**, 33-48.

Webster J. D. and De Vivo B. (2002) Experimental and modeled solubilities of chlorine in aluminosilicate melts, consequences of magma evolution, and implications for exsolution of hydrous chloride melt at Mt. Somma-Vesuvius. *Am. Min.* **87**, 1046-1061.

Webster J. D. and Rebbert C. R. (1998) Experimental investigation of H_2O and Cl- solubilities in F-enriched silicate liquids; implications for volatile saturation of topaz rhyolite magmas. *Contrib. Min. Pet.* **132**, 198-207.

Webster J. D., Kinzler R. J. and Mathez E. A. (1999) Chloride and water solubility in basalt and andesite melts and implications for magmatic degassing. *Geochim. Cosmochim. Acta* **63**, 729-738.

Westall F. and Brack A. (2018) The importance of water for life. *Space Sci. Rev.* **214**. DOI: 10.1007/s11214-018-0476-7

Witter, J. B. and Kuehner, S. M. (2004) A simple empirical method for high-quality electron microprobe analysis of fluorine at trace levels in Fe-bearing minerals and glasses. *Am. Min.* **89**, 57-63.

Wood B. J., Smythe D. J., and Harrison T. (2019) The condensation temperatures of the elements: A reappraisal. *Am. Min.* **104**, 844-856.

Wu J., Desch S. J., Schaefer L., Elkins-Tanton L. T., Pahlevan K., and Buseck P. R. (2018) Origin of Earth's water: Chondritic inheritance plus nebular ingassing and storage of hydrogen in the core. *J. Geophys. Res. Planets* **123**, 2691-2712.

Yamaguchi A., Taylor G. J., and Keil K. (1996) Global crustal metamorphism of the eucrite parent body. *Icarus* **124**, 97-112.

Yamaguchi, A., Barrat, J. A., Greenwood, R. C., Shirai, N., Okamoto, C., Setoyanagi, T., Ebihara, M., Franchi, I. A. and Bohn, M. (2009) Crustal partial melting on Vesta: Evidence from highly metamorphosed eucrites. *Geochim. Cosmochim. Acta* **73**, 7162-7182.

Zhou Q., Yin Q.-Z., Young E. D., Li X.-H., Wu F.-Y., Li Q.-L., Liu Y., and Tang G.-Q. (2013) SIMS Pb-Pb and U-Pb age determination of eucrite zircons at < 5 mu m scale and the first 50 Ma of the thermal history of Vesta. *Geochim. Cosmochim. Acta* **110**, 152-175.

Zolotov M. Y. and Mironenko M. (2007) Hydrogen chloride as a source of acid fluids in parent bodies of chondrites. *Proceedings of the 38th Lunar and Planetary Science Conference*. Lunar and Planetary Institute, Houston, TX, **38**, 2340.

Zuber M. T., McSween H. Y., Binzel R. P., Elkins-Tanton L. T., Konopliv A. S., Pieters C. M., and Smith D. E. (2011) Origin, internal structure and evolution of 4 Vesta. *Space Sci. Rev.* **163**, 77-93.

Figures

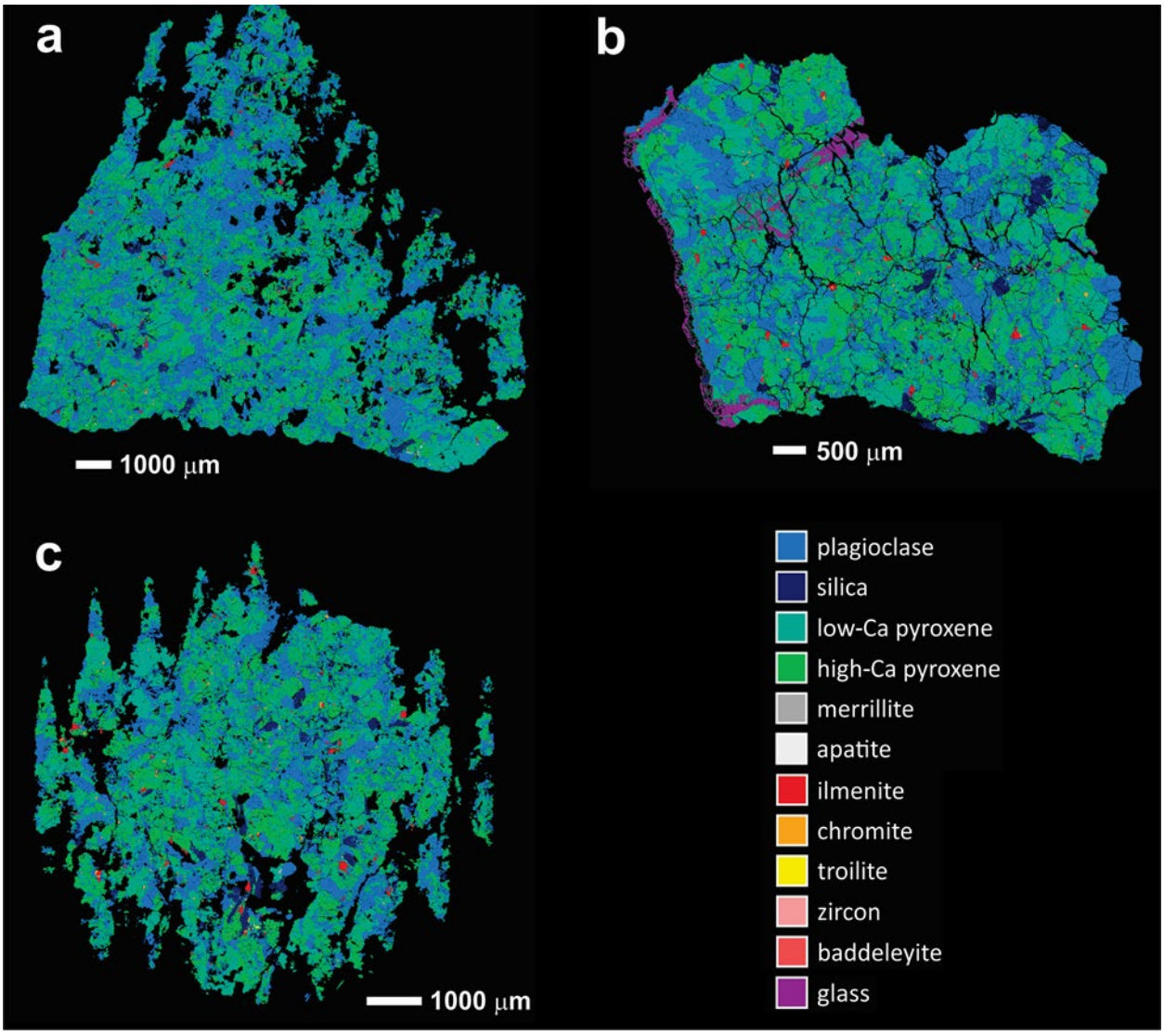

Figure 1. X-ray phase maps of three different sections of the monomict non-cumulate eucrite Berthoud, which was used to determine bulk rock F abundances from apatite modal abundances. The identity of each distinct Berthoud section used in this study is identified as a, b, or c and matches the corresponding section images in this figure. Phases are identified in X-ray maps by

the color assigned to each phase in the legend. BSE images in the same orientation as this figure are provided in Figure S1.

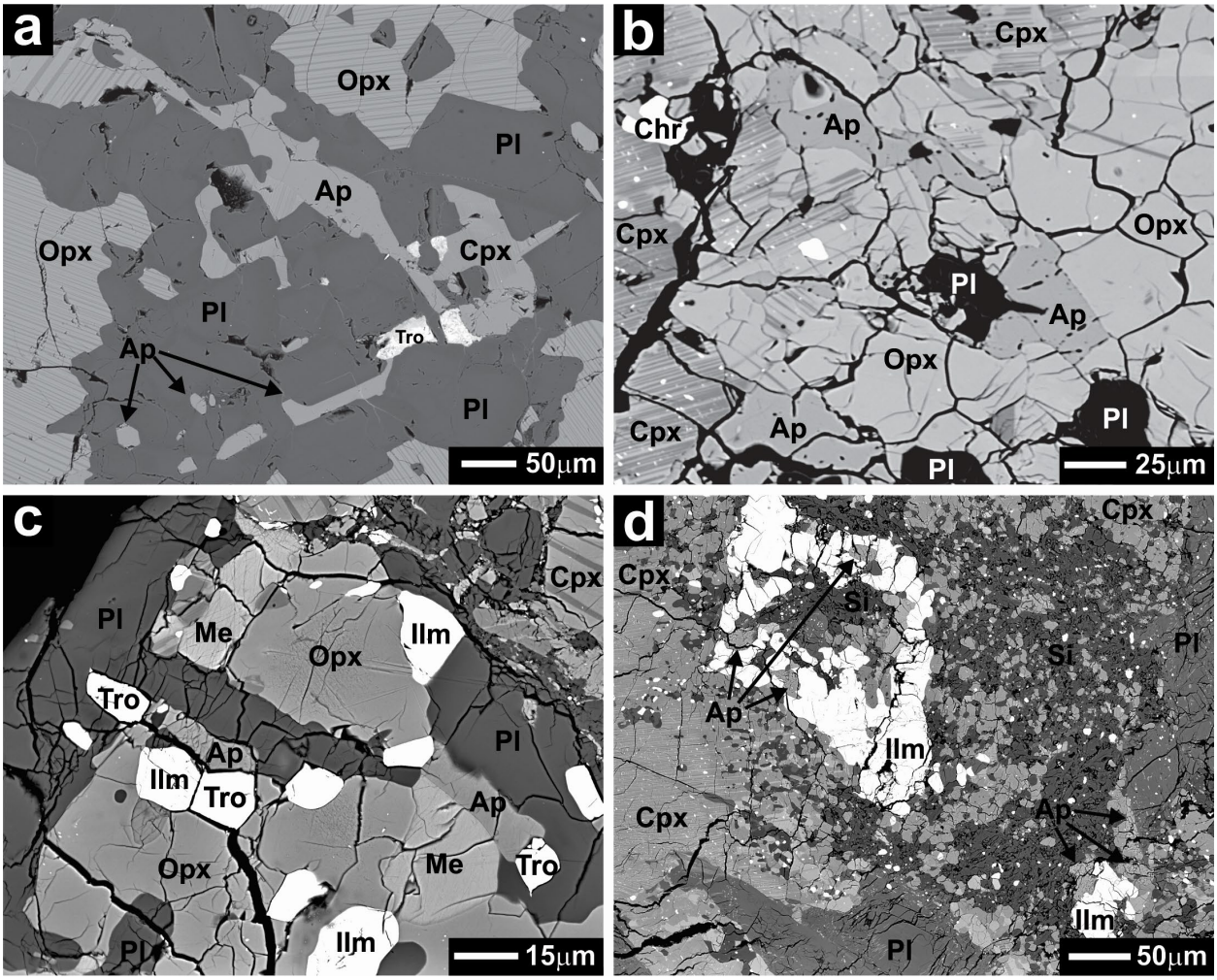

Figure 2. High-resolution back-scattered electron images of apatite from eucrites a) GRA 98098 b) PCA 91078 c) Berthoud d) Stannern. All phases present are identified, and the phase abbreviations are indicated as follows: Ap = apatite, Chr = chromite, Cpx = clinopyroxene, Ilm = ilmenite, Me = merrillite, Opx = orthopyroxene, Pl = plagioclase, Si = silica, and Tro = troilite.

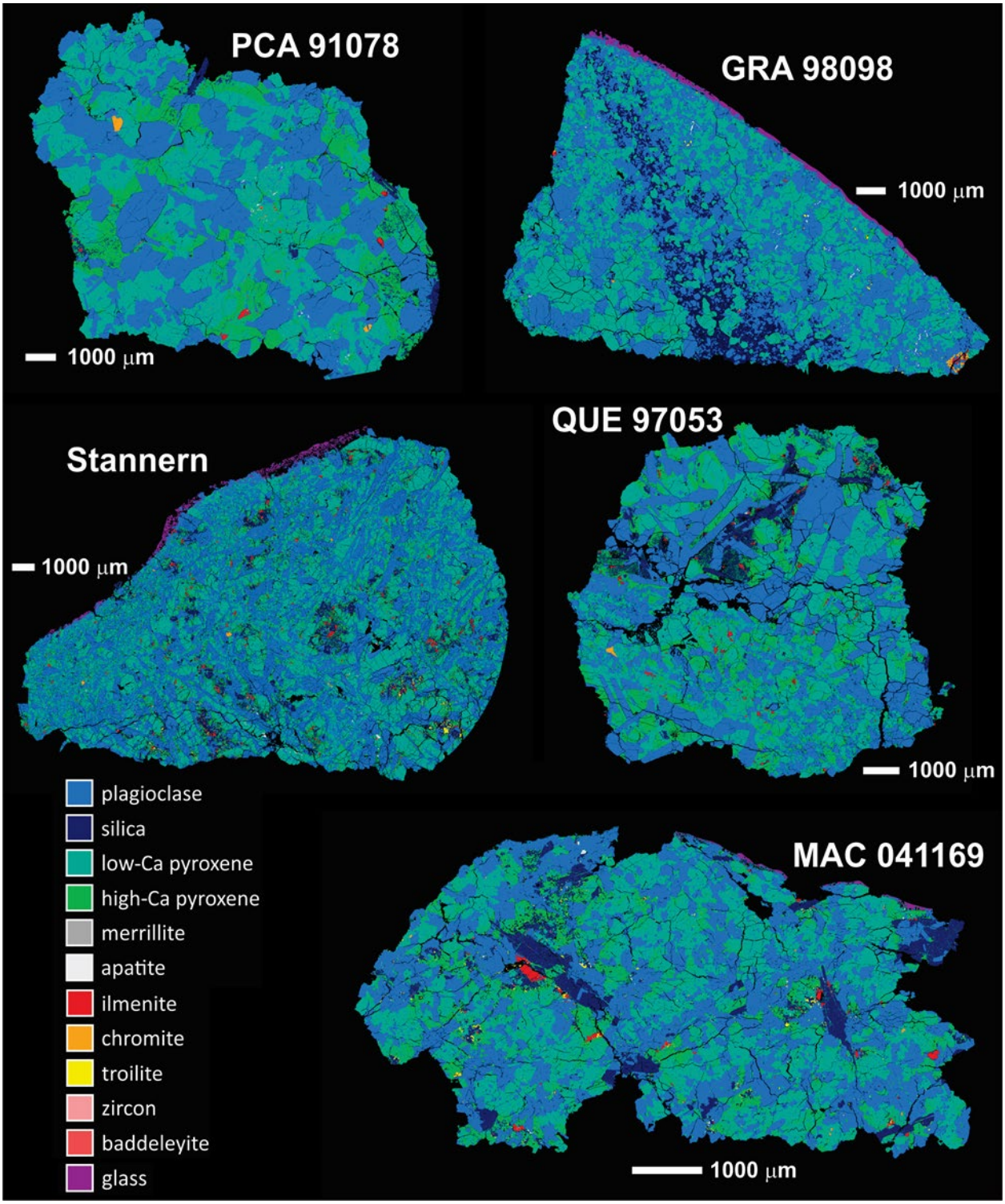

Figure 3. X-ray phase maps of the non-cumulate basaltic eucrites used to determine bulk rock F abundances from apatite modal abundances. Phases are identified in X-ray maps by the color assigned to each phase in the legend. BSE images in the same orientation as this figure are provided in Figure S2.

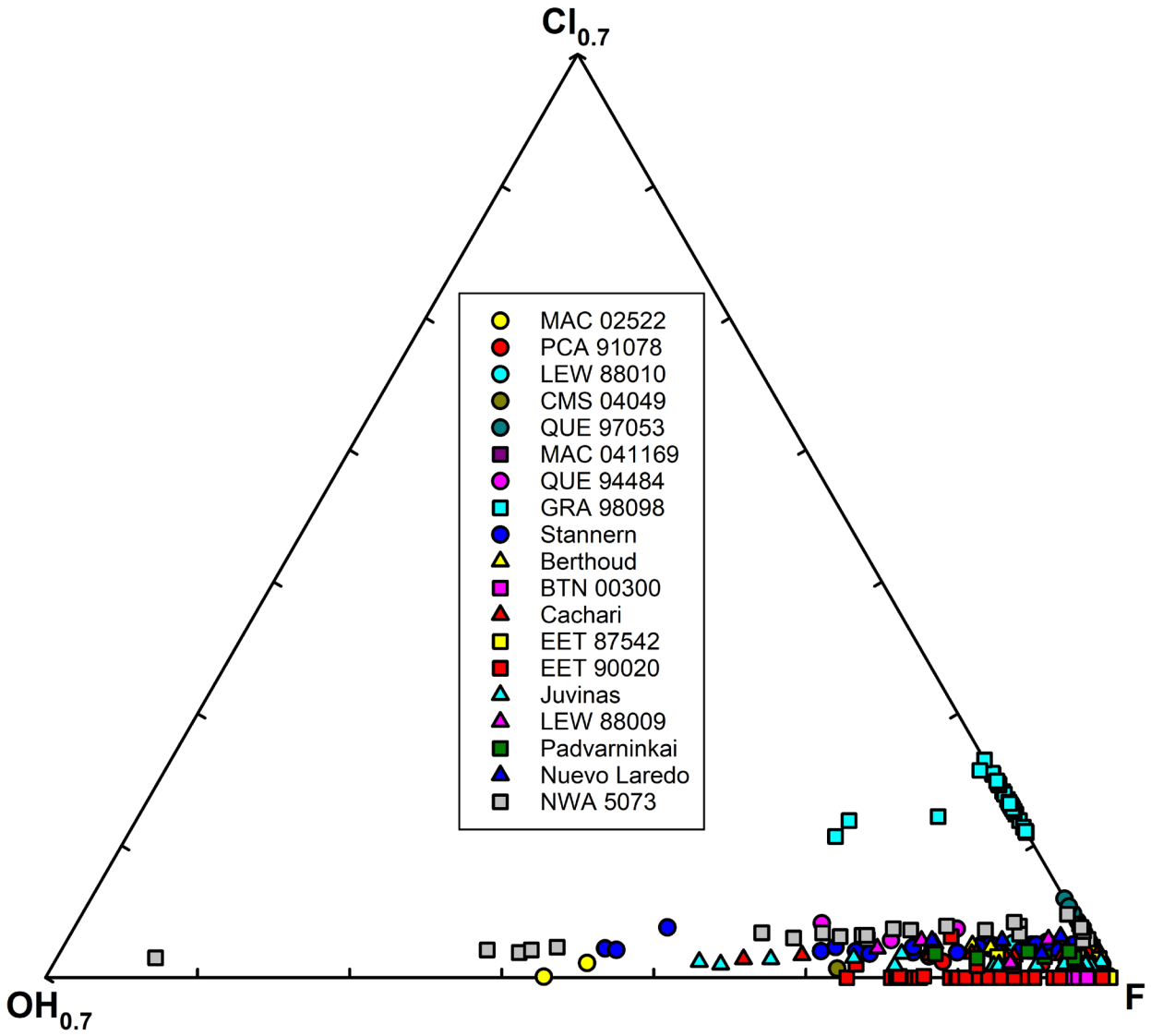

Figure 4. Truncated ternary plot of apatite X-site occupancy (mol%) from all eucrites analyzed in the present study as well as from the literature (Sarafian et al., 2013, 2014, 2017b; Ward et al., 2017; Barrett et al., 2019, 2021; Stephant et al., 2021). OH was not directly measured, so it was calculated assuming 1 – F – Cl = OH. EPMA data yielding (F + Cl) > 1 sfu are plotted along the OH-free join assuming 1 – Cl = F. All data plotted in the ternary are tabulated in Table S10.

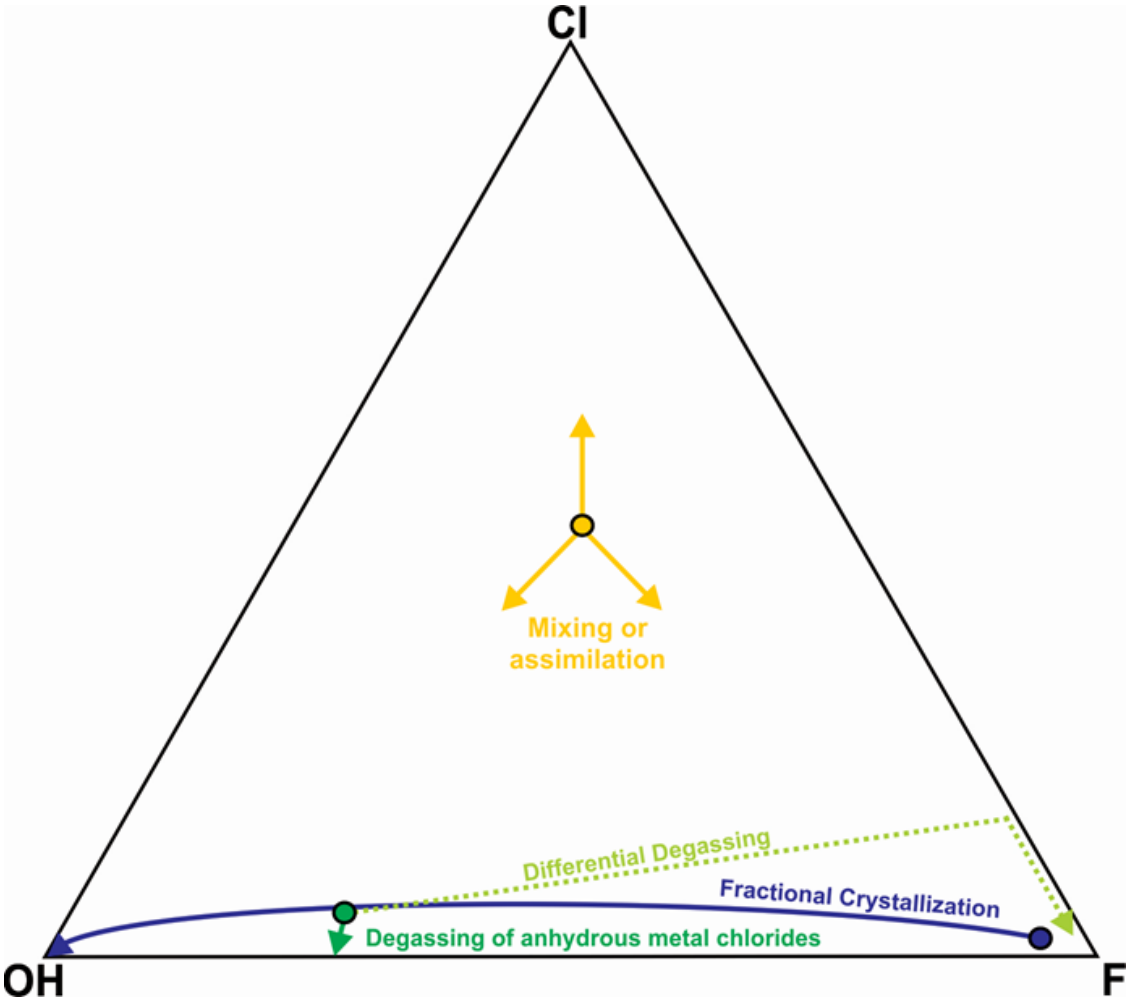

Figure 5. F-Cl-OH apatite X-site ternary diagram illustrating the evolutionary paths of apatite compositions in green for degassing, blue for fractional crystallization, and orange for mixing and assimilation. The fractional crystallization path in blue was calculated using apatite-melt exchange coefficients from McCubbin et al., (2015b) and the apatite fractional crystallization model of Boyce et al., (2014). The evolution of apatite compositions during degassing is represented by dark green and dashed light green lines. The dark green line represents degassing of anhydrous metal chlorides or Cl_2. The dashed light green line represents the path of apatite compositions during differential degassing of pure H_2 followed by degassing of metal chlorides (Ustunisik et al., 2015). The entire space enclosed by the dark green and light green lines represents the potential trajectories (from the dark green circle to the fluorapatite apex) that apatite compositions could evolve during degassing for Cl-rich hydrosaline fluids given that H and Cl typically degas together in magmatic systems on Earth (Webster and Rebbert, 1998; Webster et al., 1999; Webster and De Vivo, 2002; Webster, 2004). The orange lines represent the nearly limitless path on which apatite compositions can evolve during assimilation or mixing, as the changes in apatite compositions are controlled by the composition and abundance of the material being assimilated. This figure was adapted from McCubbin et al. (2016) to apply to Cl-poor apatite common in eucrites, mare basalts, and many terrestrial basalts (e.g., McCubbin and Jones, 2015).

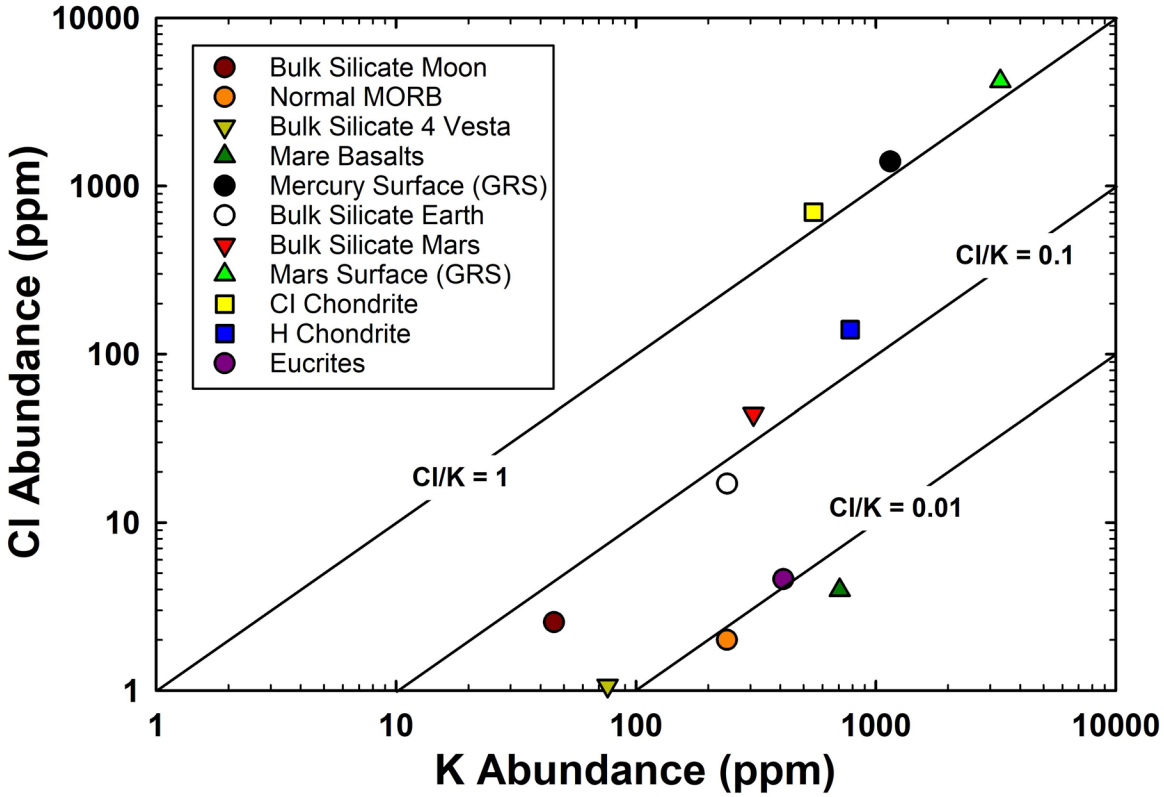

Figure 6. Relationship between Cl and K for the bulk silicate portion of 4 Vesta and other Solar System objects. Values are shown for bulk silicate Earth, Normal MORB (as exemplified by olivine-hosted melt inclusions), bulk silicate Mars, the martian surface, bulk silicate Moon, mare basalts (as exemplified by olivine-hosted melt inclusions), the surface of Mercury (value from Northern Hemisphere), eucrites, CI chondrites, and H chondrites. Lines of constant Cl/K are shown for reference. All the data plotted are tabulated in Table S13 along with their literature sources (i.e., Dreibus and Wänke, 1980; McDonough and Sun, 1995; Lodders and Fegley, 1998; Saal et al., 2002; Boynton et al., 2007; Hauri et al., 2011, 2015; Taylor, 2013; Chen et al., 2015; Evans et al., 2015; Mittlefehldt, 2015; McCubbin et al., 2016; Ni et al., 2017, 2019).

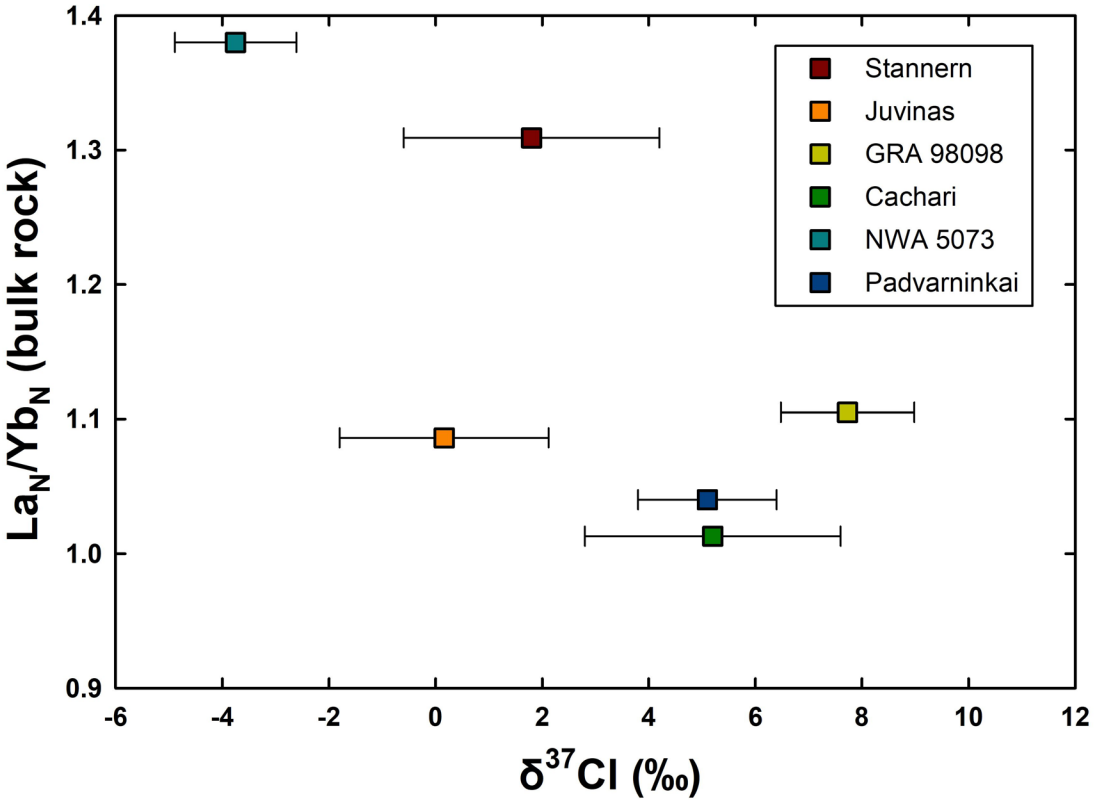

Figure 7. Plot of bulk rock La/Yb ratios in eucrites versus δ^{37}Cl values in eucrite-hosted apatite. La/Yb ratios are from Kitts and Lodders (1998), Warren et al. (2009), and Roszjar et al. (2011). Cl isotopic data are from Sarafian et al. (2017b), Barrett et al. (2019), and Barrett et al. (2021). La and Yb values normalized to CI chondrite from values in Wasson and Kallemeyn (1988). All data plotted are tabulated in Table S14.

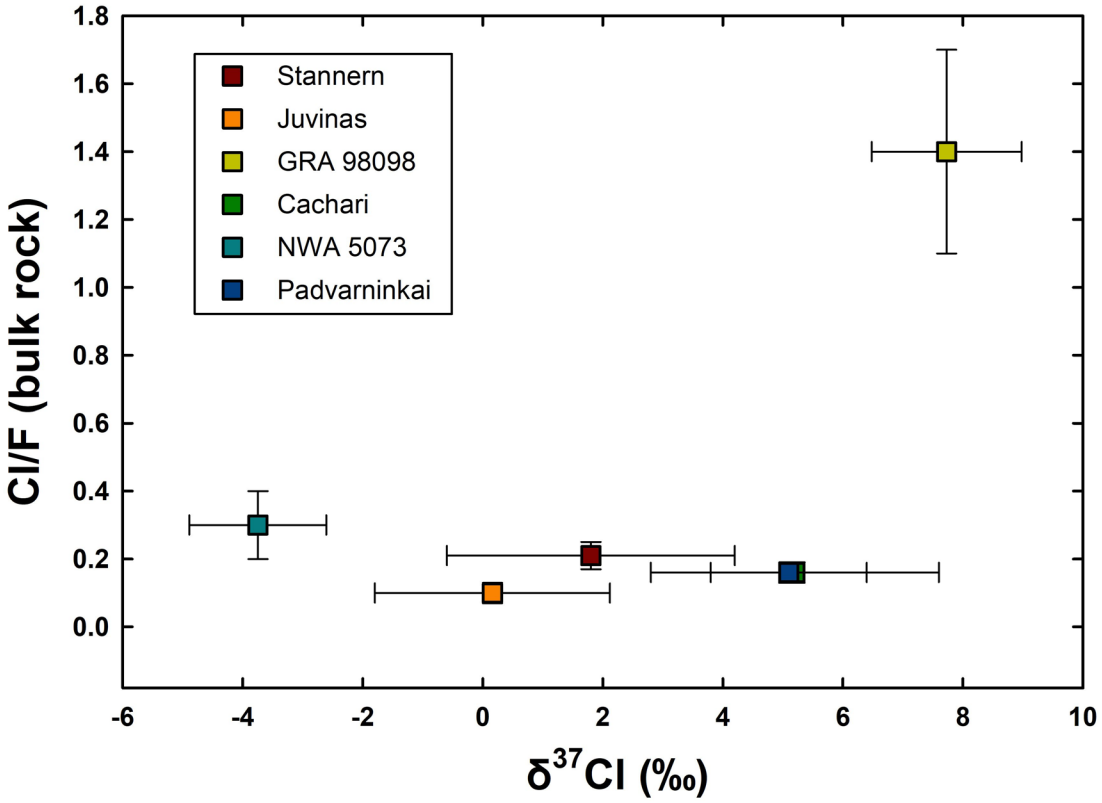

Figure 8. Plot of bulk rock Cl/F ratios in eucrites versus δ^{37}Cl values in eucrite-hosted apatite. Cl/F ratios are from this study (Table 4), and Cl isotopic data are from Sarafian et al. (2017b), Barrett et al. (2019), and Barrett et al. (2021). All data plotted are tabulated in Table S14.

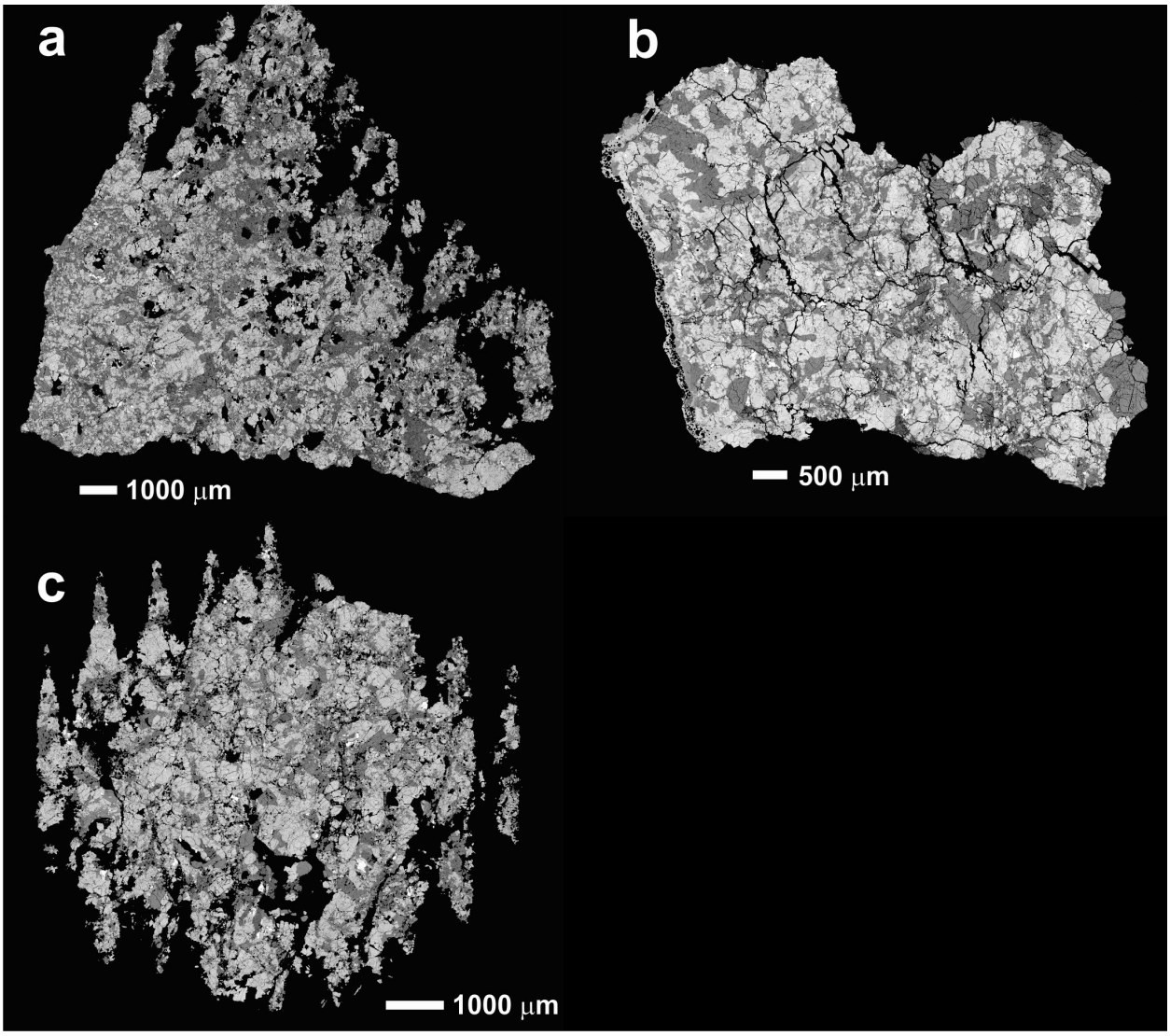

Figure S1. BSE maps of three different sections of the monomict non-cumulate eucrite Berthoud, which was used to determine bulk rock F abundances from apatite modal abundances. The samples in this figure are in the same orientation as those reported in Figure 1. The identity of each distinct Berthoud section used in this study is identified as a, b, or c and matches the corresponding section images in this figure.

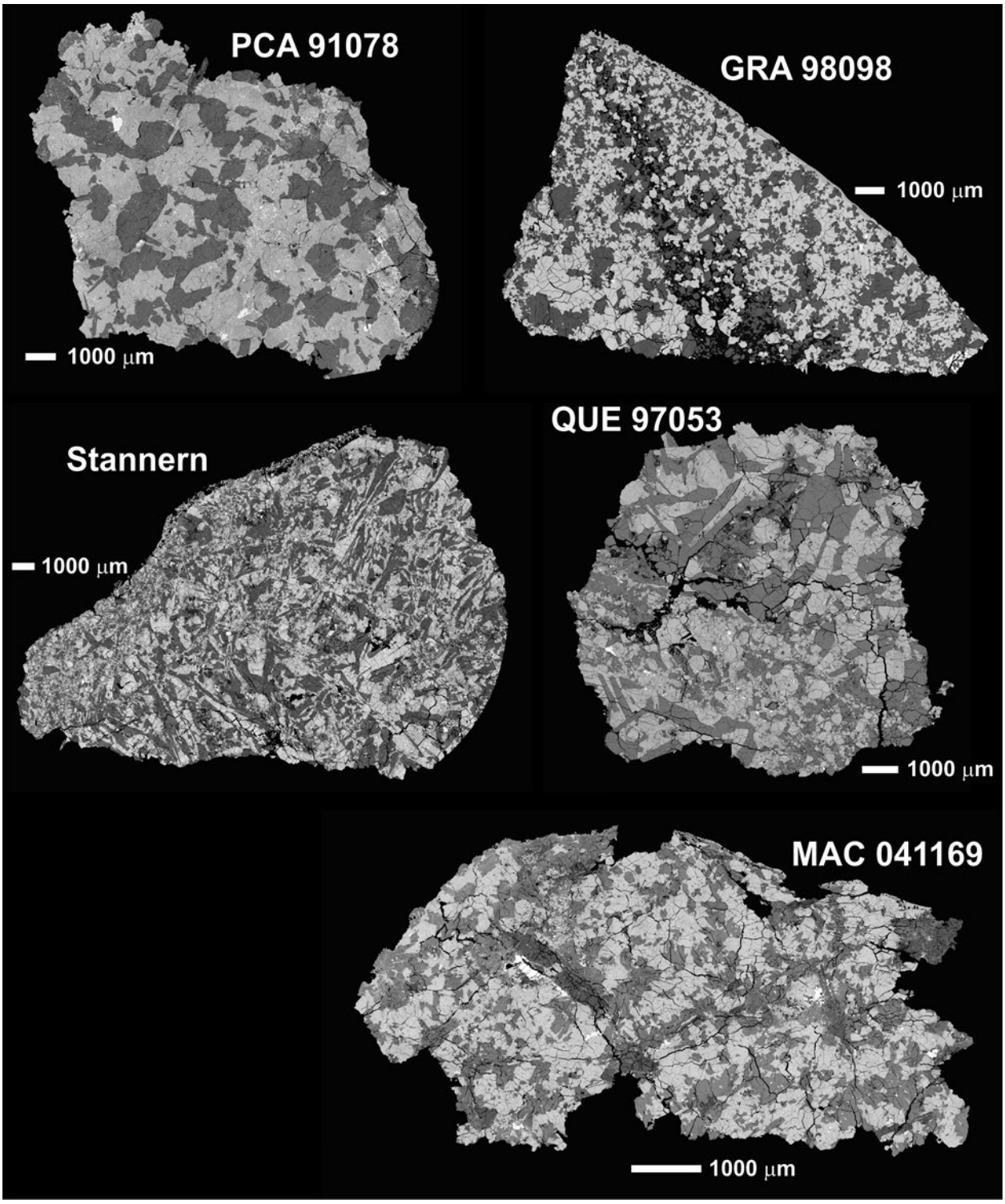

Figure S2. BSE maps of the non-cumulate basaltic eucrites used to determine bulk rock F abundances from apatite modal abundances. The samples in this figure are in the same orientation as those reported in Figure 3.

Table 1. List of eucrite samples from which apatite was analyzed during this study, including apatite data published in previous studies (i.e., Barrett et al., 2019; Barrett et al., 2016; Barrett et al., 2021; Sarafian et al., 2017; Sarafian et al., 2014; Sarafian et al., 2013; Stephant et al., 2021; Ward et al., 2017). The petrologic type of each sample along with structural occupancies of fluorine, chlorine, and hydroxyl in the apatite X-site from each sample are provided.

Name	Brecciation	Group	Avg. F* in X-site	Avg. Cl in X-site	Avg. OH in X-site†
Berthoud‡	Monomict	Stannern	0.97 (3)	0.023 (2)	0.01 (3)
BTN 00300	Unbrecciated	Main	0.96 (5)	0.00 (0)	0.04 (5)
Cachari	Monomict	Main	0.93 (7)	0.017 (2)	0.03 (2)‡
CMS 04049‡	Unbrecciated	Main	0.9 (1)	0.009 (3)	0.1 (1)
EET 87542	Monomict	Main (anomalous)	0.98 (3)	0.010 (8)	0.02 (3)
EET 90020	Unbrecciated	Main	0.91 (4)	0.002 (6)	0.14 (1)‡
GRA 98098‡	Unbrecciated	Main (anomalous)	0.86 (3)	0.14 (2)	0.1 (1)‡
Juvinas	Monomict	Main	0.90 (9)	0.011 (3)	0.07 (5)‡
LEW 88009	Unbrecciated	Main	0.94 (5)	0.025 (9)	0.04 (5)
LEW 88010‡	Unbrecciated	Stannern	0.96 (3)	0.028 (5)	0.02 (3)
MAC 02522‡	Unbrecciated	Main	0.64 (2)	0.006 (7)	0.36 (2)
MAC 041169‡	Unbrecciated	Main	0.94 (6)	0.020 (4)	0.05 (5)
Nuevo Laredo	Monomict	Nuevo Laredo	0.94 (4)	0.030 (7)	0.03 (4)
NWA 5073	Unbrecciated	Main	0.8 (2)	0.031 (8)	0.2 (2)
Padvarninkai	Monomict	Main	0.93 (4)	0.017 (2)	0.05 (4)‡
PCA 91078	Unbrecciated	Main	0.97 (4)	0.011 (5)	0.041 (5)‡
QUE 94484‡	Unbrecciated	Stannern (anomalous)	0.84 (4)	0.033 (8)	0.13 (4)
QUE 97053‡	Unbrecciated	Main	0.951 (8)	0.049 (8)	0.00 (0)
Stannern‡	Monomict	Stannern	0.94 (8)	0.022 (3)	0.08 (5)‡

All parenthetical values represent 1-sigma standard deviation of the mean (1σSDOM)

*If X-site sum exceeds 1 sfu (Tables S1-S9), F was computed assuming $X_F = 1 - X_{Cl}$

†OH computed based on stoichiometry assuming $OH = 1 – (X_F + X_{Cl})$ unless otherwise noted

‡OH determined by secondary ion mass spectrometry (SIMS), and represent average of all H_2O analyses available (i.e., Barrett et al., 2016; Barrett et al., 2021; Sarafian et al., 2017; Sarafian et al., 2014; Sarafian et al., 2013; Stephant et al., 2021)

‡Values include apatite data collected in present study

Table 2. Average electron microprobe analyses of apatite analyzed in this study

Oxide	Berthoud	CMS 04049	GRA 98098	LEW 88010	MAC 02522	MAC 041169	QUE 94484	QUE 97053	Stannern
P_2O_5	41.8 (5)	42.6 (1)	41.9 (3)	41.24 (7)	40.1 (7)	40.9 (6)	41 (2)	40.9 (6)	41.9 (8)
SiO_2	0.1 (2)	0.1 (1)	0.22 (4)	0.1 (1)	1 (1)	0.3 (3)	1 (1)	1.1 (7)	0.1 (5)
Ce_2O_3	*n.d.*	0.021 (4)	0.07 (3)	0.01 (1)	0.06 (3)	0.1 (1)	0.07 (2)	0.07 (5)	*n.d.*
Y_2O_3	*n.d.*	0.005 (6)	0.03 (1)	0.02 (1)	0.04 (6)	0.2 (2)	0.17 (9)	0.12 (5)	*n.d.*
FeO	0.5 (2)	0.7 (5)	0.5 (3)	0.67 (8)	0.9 (1)	2 (1)	2 (1)	1.0 (5)	0.4 (3)
MnO	0.04 (1)	0.03 (2)	0.08 (2)	0.03 (2)	0.07 (3)	0.07 (5)	0.07 (4)	0.054 (8)	0.03 (1)
MgO	0.02 (1)	0.017 (2)	0.05 (1)	0.03 (3)	0.07 (5)	0.05 (2)	0.07 (8)	0.04 (3)	0.03 (8)
CaO	55.5 (5)	56.27 (2)	54.6 (5)	55 (1)	54.0 (1)	53 (2)	54 (2)	53.7 (5)	55.6 (6)
Na_2O	0.01 (1)	0.03 (4)	0.01 (1)	0.11 (7)	0.01 (2)	0.12 (8)	0.01 (1)	0.00 (0)	0.006 (8)
F*	3.6 (1)	3.5 (5)	3.22 (5)	3.55 (8)	2.36 (4)	3.5 (2)	3.2 (1)	3.55 (4)	3.6 (3)
Cl	0.16 (1)	0.06 (2)	0.98 (7)	0.20 (3)	0.04 (5)	0.14 (3)	0.23 (5)	0.34 (6)	0.15 (2)
S	0.02 (4)	0.01 (1)	0.03 (2)	0.09 (1)	0.08 (5)	0.4 (2)	0.2 (3)	0.2 (2)	0.01 (2)
$-O \equiv F + Cl + S$	1.56	1.49	1.59	1.58	1.04	1.70	1.50	1.67	1.55
Total	**100.19**	**101.85**	**100.10**	**99.47**	**97.69**	**99.08**	**100.52**	**99.40**	**100.27**
N	**25**	**2**	**15**	**3**	**2**	**4**	**4**	**5**	**51**
Structural formulae based on 13 anions									
P	2.98	2.98	2.99	2.97	2.91	2.96	2.91	2.93	2.98
Si	0.01	0.01	0.02	0.01	0.09	0.03	0.12	0.1	0.00
Ce	-	0.00	0.00	0.00	0.00	0.00	0.00	0.00	-
Y	-	0.00	0.00	0.00	0.00	0.01	0.01	0.01	-
Fe	0.04	0.05	0.03	0.05	0.07	0.16	0.12	0.07	0.03
Mn	0.00	0.00	0.01	0.00	0.01	0.00	0.01	0.00	0.00
Mg	0.00	0.00	0.01	0.00	0.01	0.01	0.01	0.01	0.00
Ca	5.00	4.98	4.93	4.98	4.96	4.84	4.85	4.88	5.00
Na	0.00	0.00	0.00	0.02	0.00	0.02	0.00	0.00	0.00
∑ Cations	***8.03***	***8.02***	***7.99***	***8.03***	***8.05***	***8.03***	***8.03***	***8.00***	***8.01***
F*	0.97	0.90	0.86	0.96	0.64	0.94	0.84	0.95	0.95
Cl	0.02	0.01	0.14	0.03	0.01	0.02	0.03	0.05	0.02
S	0.01	0.00	0.00	0.01	0.01	0.06	0.04	0.03	0.00
$OH^{\dagger}$	0.00	0.09	0.00	0.00	0.34	0.00	0.09	0.00	0.03
∑ Anions	***1.00***	***1.00***	***1.00***	***1.00***	***1.00***	***1.02***	***1.00***	***1.03***	***1.00***

N – number of analyses

- signifies that a value was not computed

n.d. – abundance was not determined

All parenthetical values represent 1-sigma standard deviation of the mean (1σSDOM)

† Calculated assuming that $X_F + X_{Cl} + X_{OH} = 1$ apfu

˟ Typical detection limit for a missing component in F-rich apatite is 0.08 structural formula units (McCubbin et al., 2010b)

*If sum of X_F and X_{Cl} exceeds 1 sfu, F was computed assuming $X_F = 1 - X_{Cl}$. Raw F data reported in Tables S1-S9

Table 3. Modal abundances of phases in eucrites reported in volume percent and computed bulk rock abundances of fluorine (ppm)

Name		Berthoud	GRA 98098	MAC 041169	PCA 91078	QUE 97053	Stannern
Impact Glass		1 (2)	1.62	0.29	0.02	0.01	0.97
Minerals		99 (2)	99.38	99.71	99.98	99.99	99.03
Pyroxene		60 (2)	47.74	47.82	54.02	49.72	49.64
	Low-Ca	*36 (1)*	*45.97*	*39.72*	*44.43*	*39.33*	*44.28*
	High-Ca	*24 (2)*	*1.77*	*8.10*	*9.59*	*10.39*	*5.36*
Plagioclase		36 (3)	44.29	43.37	43.59	45.40	43.79
Silica		3.1 (0.5)	7.52	7.66	1.59	4.17	4.86
Apatite		0.034 (9)	0.118	0.079	0.061	0.021	0.152
Merrillite		0.09 (2)	0.021	0.028	0.023	0.035	0.065
Ilmenite		0.7 (1)	0.087	0.575	0.238	0.601	1.02
Chromite		0.32 (4)	0.136	0.057	0.185	0.059	0.078
Troilite		0.09 (3)	0.086	0.411	0.008	0.001	0.379
Zircon		0.002 (1)	0.000	0.003	0.070	0.002	0.005
Baddeleyite		0.001 (0)	0.001	0.006	0.219	0.001	0.008
Minerals Total		**100.34**	**100.00**	**100.00**	**100.00**	**100.00**	**100.00**
Bulk rock F (ppm)		**12 (3)**	**38 (1)**	**19 (1)**	**22 (1)**	**7.6 (1)**	**54 (5)**

Parenthetical value represents 1-sigma standard deviation of the mean (1σSDOM). Standard deviations reported for Berthoud were determined using the modal mineralogy of three different sections (Table S11), which yielded a larger uncertainty than yielded using the uncertainty on mean F abundance in apatite. Only one section was used for the other five samples, so a standard deviation was computed based on the uncertainty of mean F abundances in apatite.

Table 4. Abundances of F, Cl, and H_2O in bulk eucrites and the bulk silicate portion of 4 Vesta, along with H_2O/F and Cl/F ratio for bulk eucrites computed from apatite-based melt hygrometry and chlorometry.

Name	H_2O/F	Cl/F	F (ppm)*	H_2O (ppm)	Cl (ppm)
Berthoud	-	0.21 (4)	12 ± 3	-	2.5 ± 0.4
Béréba	-	-	53	-	-
Cachari	1.1 (6)	0.16 (3)	-	-	-
CMS 04049	-	0.08 (3)	-	-	-
EET 87542	-	0.08 (7)	-	-	-
EET 90020	5.3 (9)	0.02 (6)	-	-	-
GRA 98098	4 (4)	1.4 (3)	38 ± 1	-	52 ± 10
Haraiya	-	-	23	-	-
Jonzac	-	-	15	-	-
Juvinas	3 (2)	0.10 (3)	19.5 ± 0.7	50 ± 35	2.0 ± 0.6
LEW 88009	-	0.23 (9)	-	-	-
LEW 88010	-	0.25 (6)	-	-	-
MAC 02522	-	0.1 (1)	-	-	-
MAC 041169	-	0.19 (5)	19 ± 1	-	3.5 ± 0.9
Nuevo Laredo	-	0.28 (7)	51	-	14 ± 4
NWA 5073	-	0.3 (1)	-	-	-
Padvarninkai	2 (1)	0.16 (3)	-	-	-
PCA 91078	1.4 (3)	0.10 (5)	21.8 ± 0.9	31 ± 6	2 ± 1
QUE 94484	-	0.34 (9)	-	-	-
QUE 97053	-	0.4 (1)	7.6 ± 0.1	-	3.4 ± 0.7
Stannern	3 (2)	0.21 (4)	54 ± 5	160 ± 110	11 ± 2
Bulk Silicate 4 Vesta (BSV)			**3.0–7.2**	**3.6–22**	**0.39–1.8**

All parenthetical values represent 1-sigma standard deviation of the mean (1σSDOM)
*Literature values reported here from Kitts and Lodders (1998) for Béréba, Juvinas, and Nuevo Laredo; from Dreibus (1979) for Jonzac; and from Mittlefehldt (2015) for Haraiya.